

3

Simulations with fixed analytic potentials I: armed and barred simulations

“In the beginning the universe was created. This made a lot of people very angry and has been widely regarded as a bad move.”

– Douglas Adams, *The Hitchhikers Guide to the Galaxy*, 1978

3.1 Introduction

In order to construct synthetic emission maps, numerical simulations are needed to generate the kinetic, thermodynamical and chemical properties of the ISM gas. The simplest way to do so is to subject the gas to a number of gravitational fields that represent the various mass components of our Galaxy. This includes the central bulge, the disc in which the Earth resides, and the dark matter halo, required to reproduce the observed flat rotation curve. With these three components we can simulate a basic disc galaxy structure. The arms and bar are second order mass components that, while being weak in comparison to the bulge-disc-halo system, define the characteristic morphology of any disc galaxy. These are added through the addition of further gravitational fields, and are altered to investigate the effect of the morphology on the emission features seen in observations. The arm parameters under investigation are the rotation speed, the arm number and the pitch angle while for the bar we focus on the pattern speed and orientation. We also test different formulations of arm and bar structures, and the effect of the mass of each component.

Before including both arm and bar components together in the same simulation, the effects of each individually are studied. When creating synthetic observations it became clear that there is a significant parameter space that also needed exploring, the position and velocity of the observer.

A simple fitting routine was developed to narrow down the parameter space for each component and find the best fitting observer coordinates. This was done by the use of simple l - v maps not built using radiative transfer, and is discussed later in this chapter.

The combined arm and bar simulations, and the process of creating full radiative transfer synthetic observations, is the subject of Chapter 4.

3.2 Galactic potentials

The most important ingredient when simulating galactic scales is the inclusion of the gravitational force. For ISM gas this is dominated by the gravitational attraction of the stellar and dark matter distribution. The computation of the gravitational forces from the many billions of stars upon each SPH gas particle would be cripplingly slow for the calculation. Instead the large scale matter distribution is approximated by a continuous density distribution, significantly reducing the computational effort. This density distribution is related to the gravitational potential, Φ , by Poisson's equation, $\nabla^2\Phi = \rho_{ext}(r)4\pi G$. The force on each particle is then simply calculated from the derivative of the potential

$$\vec{f}_{ext,a} = m \frac{D\vec{v}_a}{Dt} = -\vec{\nabla}_a\Phi(\vec{r}_a) \quad (3.1)$$

which can easily be included in the SPH momentum equation (Equation 2.76). The actual form of the full galactic potential must take into account the density distribution of the Galaxy in all components. The potential is decomposed morphologically into a halo, a disc, a bulge, numerous arms, and at least one bar component

$$\Phi(\varpi, z, \phi, t) = \Phi_d(\varpi, z) + \Phi_b(\varpi, z) + \Phi_h(r) + \Phi_{bar}(\varpi, z, \phi, t) + \Phi_{sp}(\varpi, z, \phi, t) \quad (3.2)$$

where we will primarily working in cylindrical polar co-ordinates from here onwards ($\varpi^2 = x^2 + y^2$ and $r^2 = \varpi^2 + z^2$).

3.2.1 Axisymmetric potentials

While some previous studies have used potentials to produce completely flat rotation curves (e.g. Binney & Tremaine 1987), this fails to capture peak velocities near the galactic centre. This is shown in the rotation curve in Figure 3.1, using rotation curve data from Sofue (2012). Early tests with simple single component rotation curves produced l - v diagrams that were too-shallow in velocity towards the Galactic centre, because by construction these flat rotation curves are decaying in velocity rather than increasing at $R = 1\text{kpc}$.

A true Milky Way model must reproduce a semi-flat rotation curve with a magnitude of around 220kms^{-1} near the Solar position ($\approx 8\text{kpc}$). We use an axisymmetric disc, bulge and halo based on that of Pichardo et al. (2003) and Allen & Santillan (1991). The disc component is the standard Miyamoto-Nagai form (Miyamoto & Nagai 1975) with a potential of

$$\Phi_d(\varpi, z) = \frac{GM_d}{(\varpi^2 + [a_d + (z^2 + b_d^2)^{1/2}]^2)^{1/2}}, \quad (3.3)$$

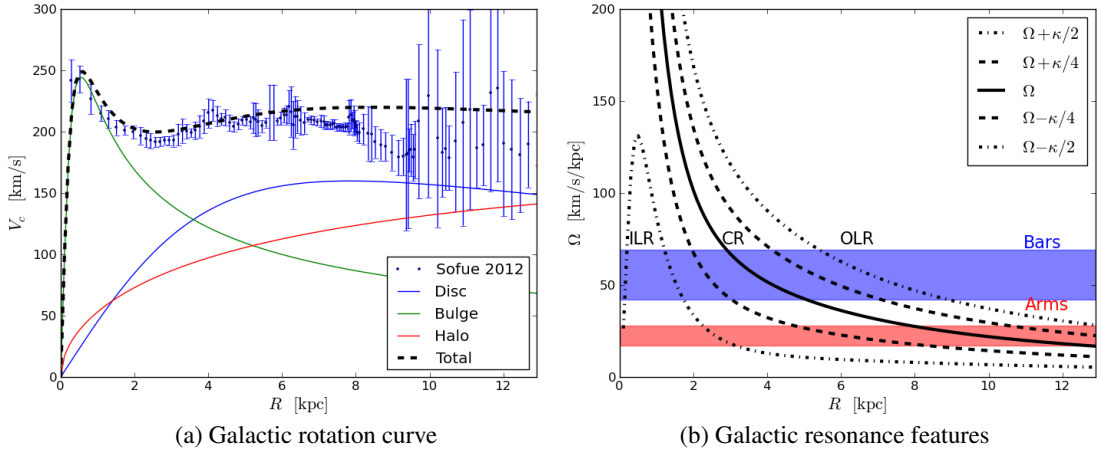


Figure 3.1: Left: rotation curve used in our simulations resulting from axisymmetric galactic potentials with observed rotation curve data from Sofue (2012). The dashed line is the combined bulge-disc-halo model from Allen & Santillan (1991) shown individually in green-blue-red respectively. Right: rotation speeds from our adopted Milky Way rotation curve. The dashed and dot-dashed lines show the 4:1 and 2:1 resonances calculated from the epicycle frequency, κ . Upper and lower shaded regions show the possible region encompassed by the arm and bar pattern speeds, with maxima and minima from Gerhard (2011).

where a_d controls the radial scaling and b_d the vertical. The bulge is described by a spherical Plummer potential (Plummer 1911),

$$\Phi_b(r) = -\frac{GM_b}{\sqrt{r^2 + r_b^2}}, \quad (3.4)$$

with r_b controlling the radial scaling, and $r^2 = x^2 + y^2 + z^2$. The spherical dark matter halo is taken from Allen & Santillan (1991),

$$\Phi_h(r) = -\frac{GM_h(r)}{r} - \frac{GM_{h,0}}{\gamma r_h} \left[-\frac{\gamma}{1 + (r/r_h)^\gamma} + \ln(1 + (r/r_h)^\gamma) \right]_r^{r_{h,max}},$$

where $r_{h,max} = 100$ kpc is the halo truncation distance and $\gamma = 1.02$. The mass inside the radius r of the halo is given by

$$M_h(r) = \frac{M_{h,0}(r/r_h)^{\gamma+1}}{1 + (r/r_h)^\gamma}. \quad (3.5)$$

The various axisymmetric potential parameters are fixed throughout all simulations to best match the rotation curve of the Milky Way and are given in Table 3.1, taken from Allen & Santillan (1991). This same bulge-disc-halo model was found to also provide a good match with more recent rotation curve measurements in Irrgang et al. (2013) but with slightly different values than those in Table 3.1. We choose to retain our values in Table 3.1 however, as they provide a better match to the inner Galaxy while keeping the rotation curve high in the outer disc. There are numerous other potential sets in the literature we could have chosen to represent the axisymmetric component, and we will in fact use a slightly different model in Chapter 5.

This is a very idealised and simplified perception of the gravitational field of our Galaxy.

Term	Description	Value
M_d	Disc mass	$8.56 \times 10^{10} M_\odot$
M_b	Bulge mass	$1.40 \times 10^{10} M_\odot$
$M_{h,0}$	Halo mass	$10.7 \times 10^{10} M_\odot$
a_d	Disc radial scale length	5.30 kpc
b_d	Disc vertical scale length	0.25 kpc
r_b	Bulge radial scale length	0.39 kpc
r_h	Halo radial scale length	12.0 kpc

Table 3.1: Fixed Galactic axisymmetric potential parameters used to reproduce the observed rotation curve.

The gravitational attraction of the gas disc has been neglected, which is assumed to be negligible compared to that of the stellar disc. The stellar disc is a single component system, though there has been some evidence that the stellar disc is composed of two distinct populations (Gilmore & Reid 1983; Bovy et al. 2012). The bulge is assumed to be spherical, though there is evidence that the bulge is flattened, and non-axisymmetric (e.g. Dwek et al. 1995, McWilliam & Zoccali 2010). For simplicity we assume all asymmetry towards the Galactic centre is reproduced by the bar, and that the spherical bulge is sufficient to reproduce the features of the rotation curve. As little is known about the dark matter structure of our Galaxy, a spherically symmetric model that provides a good fit to the rotation curve is assumed sufficient. Another feature of minor importance to the work presented here is the warp of the Galactic disc (e.g. Kalberla et al. 2007), though as the warping is minor within $R < 20$ kpc it is assumed to be of little importance.

3.2.2 Spiral arm potentials

The spiral and bar features are produced by subjecting the gas to further stellar potentials. When using fixed analytic potentials the structure of the Milky Way is assumed to be that of a grand design galaxy, driven by some stable stellar density wave. The potentials used here have a constant strength throughout the simulation. The radial extent of structures is determined by the location of the inner and outer Linblad resonances, ILR and OLR, which are in turn determined by the pattern speed of the density wave, Ω_{bar} or Ω_{sp} . The frequencies resulting from our rotation curve are shown in the right panel of Fig. 3.1. For example, a 4-armed spiral perturbation with a pattern speed of $20 \text{ km s}^{-1} \text{ kpc}^{-1}$ has ILR, OLR and CR located at a radius 7.0, 14.4 and 10.9 kpc respectively, shown by where the $\Omega \pm \kappa/4$ and Ω lines cross $20 \text{ km s}^{-1} \text{ kpc}^{-1}$ in Fig. 3.1.

Bar and spiral potential parameters we choose to vary are summarised in Table 3.2. These include the pitch angle of spiral arms (α), the number of spiral arms (N), and the pattern speed of the bar and arms (Ω_b, Ω_{sp}). We also investigate the effects on altering the strength of the potential perturbations, though we only use two separate values for the arm and bar components. The orientation of the bar/arm features to the observer (l_{obs}), and the observer's velocity and Galactocentric distance (V_{obs}, R_{obs}) are also investigated but these are varied during the construction of l - v maps. Our choice of parameters is broad and numerous to allow for an unbiased study, with as little recourse as possible to previous findings. There is both observational and numerical evidence for different pattern speeds for the arm and bar components in our Galaxy (e.g. Gerhard 2011 and

Term	Description	Values
Ω_b	Bar pattern speed	20, 40, 50, 60 , 70 km s ⁻¹ kpc ⁻¹
θ_b	Bar orientation	0°, 10°, ..., 50°, 60°
Ω_{sp}	Arm pattern speed	10, 15, 20 , 25, 30 km s ⁻¹ kpc ⁻¹
α	Arm pitch angle	5°, 10° , 12.5° , 15° , 20°
N	Number of arms	2, 4
$ \Phi_{sp} $	Relative arm potential strength	×1, ×2
R_{obs}	Radial position of the observer	7, 7.5, 8, 8.5, 9 kpc
V_{obs}	Circular velocity of the observer	200, 205, ..., 225, 230 km s ⁻¹
l_{obs}	Azimuthal position of the observer	0°, 10°, ..., 350°, 360°

Table 3.2: Variable parameters of the simulations, including those of the arm/bar potentials and those used in defining the observer co-ordinates. Parameters in bold define the refined parameter space used in calculations with both bar and arm potentials in Chapter 4.

Sellwood & Sparke 1988), though some simulations are performed with equal speeds for both components.

In Dobbs et al. (2006) a logarithmic spiral potential from Cox & Gómez (2002) was used, hereafter referred to as CG arms. This is our primary arm model, and takes the form

$$\Phi_{sp}(r, \phi, z) = 4\pi G h_z \rho_0 \exp\left(-\frac{r-r_0}{R_s}\right) \sum_n^3 \frac{C_n}{K_n D_n} \left[\operatorname{sech}\left(\frac{K_n z}{\beta_n}\right) \right]^{\beta_n} \cos\left(N\left[\phi - t\Omega_{sp} - \frac{\ln(r/r_0)}{\tan(\alpha)}\right]\right) \quad (3.6)$$

where

$$K_n = nN/r \sin(\alpha), \quad (3.7)$$

$$D_n = \frac{1 + K_n h_z + 0.3(K_n h_z)^2}{1 + 0.3K_n h_z}, \quad (3.8)$$

$$\beta_n = K_n h_z (1 + 0.4K_n h_z), \quad (3.9)$$

and the constants are the same as those used in Dobbs et al. (2006), namely $h_z = 0.18$ kpc, $R_s = 7$ kpc, $r_0 = 8$ kpc, $C = (8/3\pi, 1/2, 8/15\pi)$ and a fiducial spiral density of $\rho_0 = 1$ atom cm⁻³. These spiral arms take the form of a three part sinusoidal perturbation that exponentially decays with increasing radius. The three component sum nature of the potential makes the potential relatively flat in the inter-arm region compared to a purely sinusoidal case, and more strongly peaked (Cox & Gómez 2002).

The logarithmic spiral perturbation of Pichardo et al. (2003) is also included in our calculations due to its apparent effectiveness at creating four armed spiral patterns in the ISM gas from only a two armed stellar potential (Martos et al. 2004), which has been proposed by some to be the reason behind the 4/2 armed model dichotomy in the literature (Churchwell et al. 2009). This potential is substantially more complicated and represents the spiral arms as a superposition of oblate spheroids (Schmidt 1956; Ollongren 1967) whose loci are placed along a modified

logarithmic spiral arm function of the form

$$f(r) = \frac{1}{N} \ln \left(1 + (r/r_o)^N \right) \cot(\alpha) \quad (3.10)$$

instead of the standard shape function of

$$f(r) = \ln(r/r_o) \cot(\alpha) \quad (3.11)$$

stemming from the $r = r_o e^{\tan(\alpha)\phi}$ logarithmic nature. This allows for a smooth turn off from a spiral to bar-like structure at some small radius. Each of the spheroids themselves have an linear internal density profile of $\rho_{ss}(a, r) = p_0(a, r) + ap_1(a, r)$ where a is the distance to the spheroids centre. The authors suggest the density parameters $p_0(r)$ and $p_1(r)$ themselves follow either a linear or logarithmic decay with increasing distance, r , from the Galactic centre. They find the logarithmic decrease and lower arm mass is most effective at creating secondary arm structures in the gas, so we adopt the same here. This potential had to be constructed using the work of Ollongren (1967) and Schmidt (1956) as it was not given in Pichardo et al. (2003). As this was a discrete analytic function, a derivative could easily be computed for force calculations. The full solution for the forces in the radial and azimuthal directions is given in Appendix B.1. This potential is referred to as the PM model for the remainder of this thesis.

Upon integration into the SPH code it became clear that this potential was creating a bottleneck in the run-time of the simulation. This is a result of the sum of forces over each individual spheroid in the arms, which proved to be very time-consuming at high resolutions. To combat this a 3-dimensional grid of the potential was written to a file to be read in at the start of the simulation and used throughout for all ensuing force calculations. Forces were then computed by finite differences between the potential in neighbouring grid-cells, and linear interpolation inside each cell. Sufficient resolution of the grid was determined by comparison to the analytic form of the forces. The rotation of the arms was produced by simply rotating the particles to the frame of the arms, evaluating the forces, rotating the force field back to the position of the particle and applying it (also detailed briefly in Appendix B.2).

All of our arm models are assumed to be logarithmic, with constant pitch angles and are evenly spaced azimuthally. However, as mentioned in Chapter 1, there is evidence of the individual arms of the Milky Way being best fit by different pitch angles.

3.2.3 Bar potentials

The dynamics in the inner Galaxy ($R < 4\text{kpc}$) is believed to be dominated by a bar structure, in essence a spheroid elongated along one axis parallel with the Galactic disc. Models for the bar vary greatly in complexity. These range from those tuned to match a specific density profile constrained by observations, to ones that simply give a trough of gravitational potential every π radians. Several separate bar potentials have been tested to see which functional representation best matches the l - v features of our Galaxy. The first is a commonly used sinusoidal perturbation

of the Galactic disc. We employ the specific form of Wada & Koda (2001);

$$\Phi_{bar}(r, \phi) = \Phi_0 \cos(2[\phi + \Omega_b t]) \frac{(r/r_c)^2}{((r/r_c)^2 + 1)^2}, \quad (3.12)$$

where $\Phi_0 = \epsilon V_0^2 \sqrt{27/4}$, $\epsilon = 0.05$ and $V_0 = 220 \text{ km s}^{-1}$. We employ two different values of the bar core radius, r_c , either 2 kpc or $\sqrt{2}$ kpc (used in Wada et al. 1994 and Wada & Koda 2001 respectively). We will refer to these as the WK and WKr2 bars respectively throughout this manuscript. A measurement of the inner drop off radius of the bar potential, r_c here also determines the strength of the potential, and so these values enable us to investigate the effect of the strength of the bar. The models of Dehnen (2000) and Minchev et al. (2007) were also investigated, but showed little difference to the bar above so were not used beyond initial testing.

Another bar we employ is that of Long & Murali (1992), referred to hereafter as the LM bar. The authors provide a bar model that is simply a softened line of gravitational potential. While not physically a bar, i.e. not the result of some density profile, the effect on the gas is still that of a non-axisymmetric perturbation. This potential is aligned with the x-axis by definition so we apply co-ordinate transforms to the positions and accelerations to simulate the rotation of the bar. The potential is given by

$$\Phi_{bar}(x, y, z) = \frac{GM_{bar}}{2a} \ln\left(\frac{x - a + T_-}{x + a + T_+}\right), \quad (3.13)$$

where $T_{\pm} = [(a \pm x)^2 + y^2 + (b + \sqrt{c^2 + z^2})^2]^{1/2}$, with a, b and c roughly corresponding to the bar semi-major and minor axes respectively. We adopt a bar mass of $6.25 \times 10^{10} M_{\odot}$ as used by Lee et al. (1999) for the same potential. This bar has the advantage of a controllable minor-axis length while maintaining a simple analytical form.

Both of these models are simplistic in design, and there have been several studies that have managed to fix specific density distributions to the bar. These include the ‘‘Dwek’’ (Dwek et al. 1995; Zhao et al. 1996), ‘‘Ferrers’’ (Ferrers 1887; Kim et al. 2012) and ‘‘Freeman’’ (Freeman 1966) bar models, though many different prescriptions exist in the literature (e.g. Pichardo et al. 2004). A significantly more complex bar model was included in our investigation based on a peanut/boxy morphology from Wang et al. (2012). As this density profile is so complex the authors expand the potential and density into a set of orthogonal basis pairs (Hernquist & Ostriker 1992; Zhao et al. 1996), of the form

$$\Phi_{bar}(r, \phi, \theta) = -\frac{GM_{bar}}{r_{bar}} \sum_{n,m,l} A_{nlm}(\rho_{bar}) \Phi_{nlm}(r, \phi, \theta) \quad (3.14)$$

where Φ_{nlm} is composed of spherical associated Legendre and Gegenbauer polynomials and is independent of the actual density profile (see Wang et al. 2012 for specific formulation). The A_{nlm} coefficients contain the density information, and are constants independent of position. The coefficients provided by (Wang et al. 2012) have a built-in bulge. To keep the rotation curve consistent with the rest of our calculations the coefficients are re-computed just using the bar component. As this potential is an extremely complex function the forces are evaluated using finite differences in a pre-made potential grid (as in the PM arm model).

The final bar model used is that of Vogt & Letelier (2011). This model is similar to the

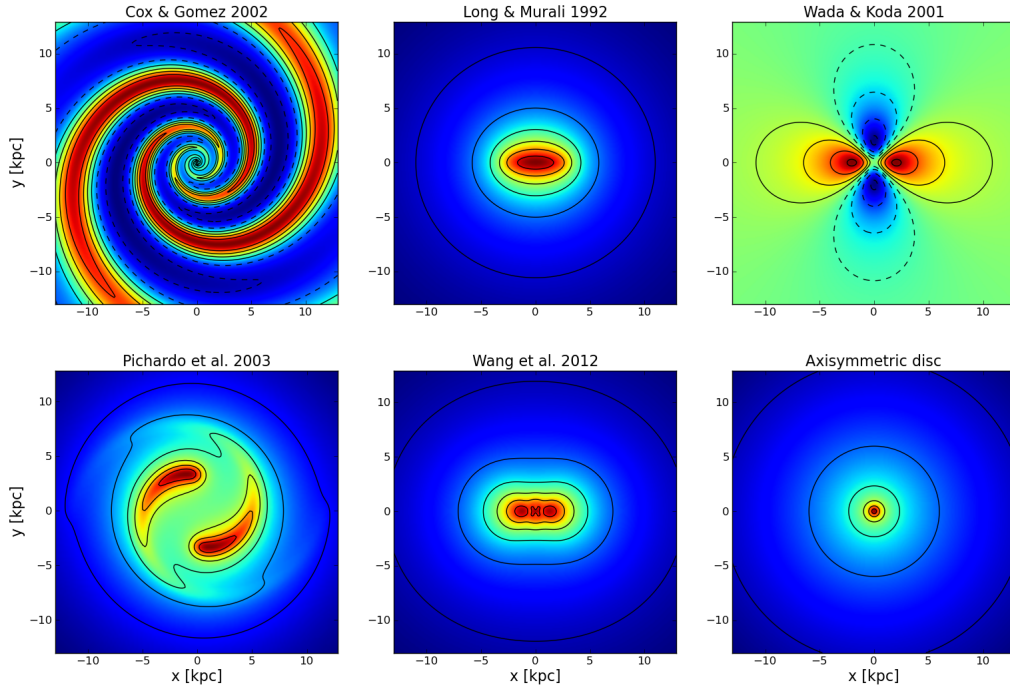


Figure 3.2: Various potentials used in our simulations. From top left to bottom right; Cox & Gómez (2002), Long & Murali (1992), Wada & Koda (2001), Pichardo et al. (2003), Wang et al. (2012) and our axisymmetric model adapted from Allen & Santillan (1991). Relative potential strength (normalised for each model) is indicated by colour scheme, with equipotential contours shown as solid (troughs) and dashed (peaks) lines.

LM bar but is adapted to allow to subtle bending into an “S” shape. This allows a bar that could smoothly tail off as it rotates, rather than abruptly cut-off at the end of the bar. The authors also provide a prescription for a “C” shape, but it is not used in this study.

Early tests were performed with the combined bar-arm model of Khoperskov et al. (2013) where a strong 2 arm, weak 4 arm, and inner bar structures are all combined into a single potential that rotates at some global pattern speed. While a reasonable approximation for the global structure of the Galaxy, this model was quickly abandoned due to its simplicity and built in assumptions of the Galactic morphology.

The gravitational fields of each of our primary potentials, including the full axisymmetric component, are shown in Figure 3.2. Here the differences between the arm potentials becomes clear. The CG arms are persistent throughout the entire disc, while the PM arms are strongest around $R = 5\text{kpc}$ and decay rapidly towards the edge of the disc. The bar structures also show some striking differences. The peanut/boxy nature of the Wang et al. (2012) is only slightly visible, but is clearer if the vertical direction. The odd appearance of the WK bar is due to it being a sinusoidal perturbation to the Galactic disc with peaks/troughs every $\pi/2$ radians, with no corresponding physical density profile¹.

¹The potentials used can be split into two distinct categories; those that perturb the gravitational field of an existing

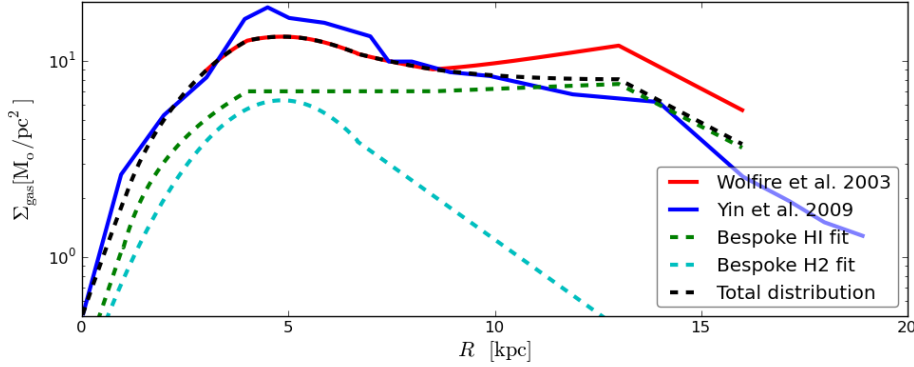


Figure 3.3: Initial surface density profile used in our simulations, shown as the black dashed line. The red line is the model of Wolfire et al. (1995) and the blue line is the data from Yin et al. (2009), taken from Boissier & Prantzos (1999), which extends to the Galactic centre. Note that we only set gas out to a radius of 13 kpc.

3.3 Setting the initial conditions

The ISM gas is initially distributed in the Galactic plane, with a disc height of 0.4 kpc. The initial vertical distribution is of little importance, as all the gas falls into a disc of height 0.1 kpc after only 50 Myrs of evolution. The initial surface density profile is chosen to match observational data. This is based on the functional form of Wolfire et al. (2003). We impose a flat distribution instead of the slightly increasing density profile in the 8.5-13.0 kpc region so that our surface density is not increasing near the edge of the disc. Some observations suggest the distribution is effectively flat from 5-15 kpc (see Kalberla & Kerp 2009 and references therein). We also extrapolate the density profile to the Galactic centre, using the data from Yin et al. (2009). Our adapted surface density function is thus for HI

$$\Sigma_{\text{HI}}(R) = 1M_{\odot} \text{pc}^{-2} \times \begin{cases} 0.2 \exp(R_k/0.7) & 0 \leq R_k < 1 \\ 1.4R_k - 0.6 & 1 \leq R_k < 4 \\ 5 & 4 \leq R_k < 8.5 \\ 4.15 + 0.1R_k & 8.5 \leq R_k < 13 \end{cases} \quad (3.15)$$

and for H₂

$$\Sigma_{\text{H}_2}(R) = 1M_{\odot} \text{pc}^{-2} \times \begin{cases} 4.5 \exp\left(-\left[\frac{R_k - 4.845}{2.6545}\right]^2\right) & 0 \leq R_k < 6.67 \\ 2.5 \exp\left(\frac{6.97 - R_k}{2.89}\right) & 6.67 \leq R_k < 24 \end{cases} \quad (3.16)$$

where $R_k = R/1\text{kpc}$. Both are added together to give the distribution in Figure 3.3. Gas in our simulations is set between 0 and 13 kpc. To actually place the gas the surface density profile is used as a PDF (probability density function), which is then integrated to create a CDF (cumulative distribution function), which is then tabulated and inverted to allow the drawing of semi-random particle positions according to the surface density shown in Fig. 3.3. The azimuthal position is

Galactic disc (WK and CG models), or those that add an extra mass component to the system (LM and PM models). While this implies the latter category will cause an overall increase in the rotation curve, the effect of this was seen to be marginal due to the weak nature of all the potentials used here.

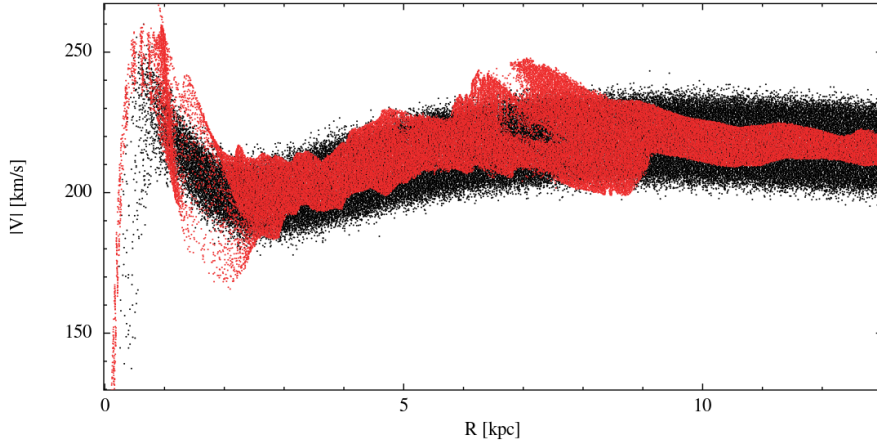


Figure 3.4: Initial rotation curve from an ISM simulation of 1 million SPH particles (black points) and after 300Myrs embedded in a barred-spiral potential (red points). Regions of higher dispersion coincide with arm and bar resonance regions.

drawn from a uniform random distribution from $0-2\pi$. Our choice of limiting our disc to 13 kpc ensures the major spiral features recorded in the literature are included as far out as the Outer and Perseus arms. Though there is some evidence for weak spiral structure extending to 20 kpc (Levine et al. 2006), this would have required a large increase in particle number to achieve the same resolution, whilst any features at such large radius would have little influence on our results due to the low gas density in the far outer disc. Integration of this surface mass distribution gives a total gas mass of approximately $8 \times 10^9 M_{\odot}$, corresponding to an average ISM density of approximately 1 g cm^{-3} or $15 M_{\odot} \text{ pc}^{-2}$. This is used as our fiducial disc mass, though simulations are also performed with lower values to test the effect of the gas mass.

Initial velocities are seeded from the axisymmetric potentials directly via

$$v_c^2(R) = R \frac{d}{dR} [\Phi_d + \Phi_h + \Phi_b] \quad (3.17)$$

which is then split between v_x and v_y to ensure a purely circular orbit at $t = 0\text{Myrs}$. A random velocity perturbation is added to each component drawn from a Gaussian distribution of width 5 km s^{-1} , so that $\vec{v}(t = 0\text{Myrs}) = (v_c \sin \phi + \delta v_x, -v_c \cos \phi + \delta v_y, +\delta v_z)$. An example of a rotation curve from a barred-spiral model is shown in Figure 3.4 where the black points show the rotation at $t = 0\text{Myrs}$ and red points after 300Myrs of evolution in a barred-spiral potential. The rotation curve at later times does not deviate strongly from that initially, but there is considerable dispersion at the resonance radii of the bar and spiral features ($R = 2\text{kpc}$ and $R = 8\text{kpc}$).

The remaining value needed to set up the SPH particles is the initial gas temperature (which determines the internal energies). Obviously this will have a large effect on isothermal simulations, where the internal energy will not change and will dictate the efficiency of gas mixing. In adiabatic+cooling simulations it is less obvious how this would effect the evolution of the system. Tests were performed with gas initially at 10000K and 200K with active ISM chemistry and cooling. Gas is seen to cool very fast in the hotter simulation, and after 15Myrs has reached the same magnitudes as the colder simulation. After 100Myrs there is only minimal differences between

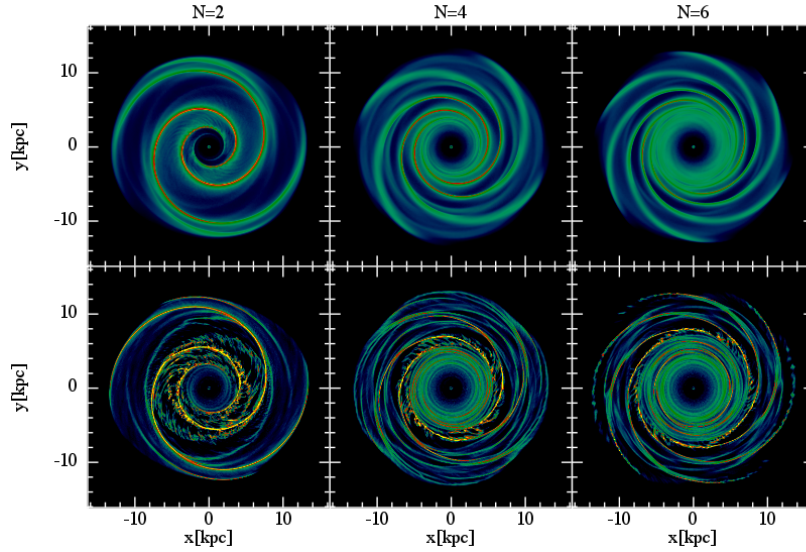


Figure 3.5: Isothermal calculations with $T = 10000\text{K}$ (top) and $T = 200\text{K}$ (bottom) for $N = 2, 4, 6$ armed models using the CG potential.

the initially hot and cold disc. As the simulations are normally ran for at least 200Myrs (to ensure all particles and potentials have conducted at least one full rotation) the initial temperature of the gas is assumed unimportant. To avoid spurious side-effects of the rapid cooling of an initially hot disc the initial temperature of the gas particles is set to $T = 200\text{K}$.

Our fiducial simulation resolution is 5 million SPH particles. Tests were made with 1-10 million particles. Morphological differences were minor between the different resolutions, but the amount of CO created was considerably reduced with lower resolutions. 5 million particles was found to be a good trade off between CO production and run-time. This was further supported by tests with l - v maps, where the additional emission from the increase to 10 million particles was marginal compared to the increase from 1-5 million. See Section 4.4.1 for a more in-depth analysis of the effect of simulation resolution.

3.4 Isothermal simulations: testing the potentials

In this section the general features of the potentials in isothermal calculations are shown. The cooling and chemically active calculations take considerably longer to run, so isothermal calculations provide a good test-bed for the various potentials before full production calculations are made. Simulations presented here are at a resolution of 1 million SPH particles. The effect of varying temperature in simple isothermal calculations is shown in Figure 3.5, where the top row shows calculations at $T = 10000\text{K}$ and the bottom at $T = 200\text{K}$ for various numbers of arms using the CG model at $\Omega_{sp} = 20\text{km s}^{-1} \text{kpc}^{-1}$. The hotter calculations are much “cleaner”, in that the gas is clearly smoothly tracing out the spiral potential, producing regions of high density in the bottom of the potential wells. The colder simulations reach much higher densities but also have a large amount of supplementary structure. The $N = 4$ model in particular has a large amount of arm

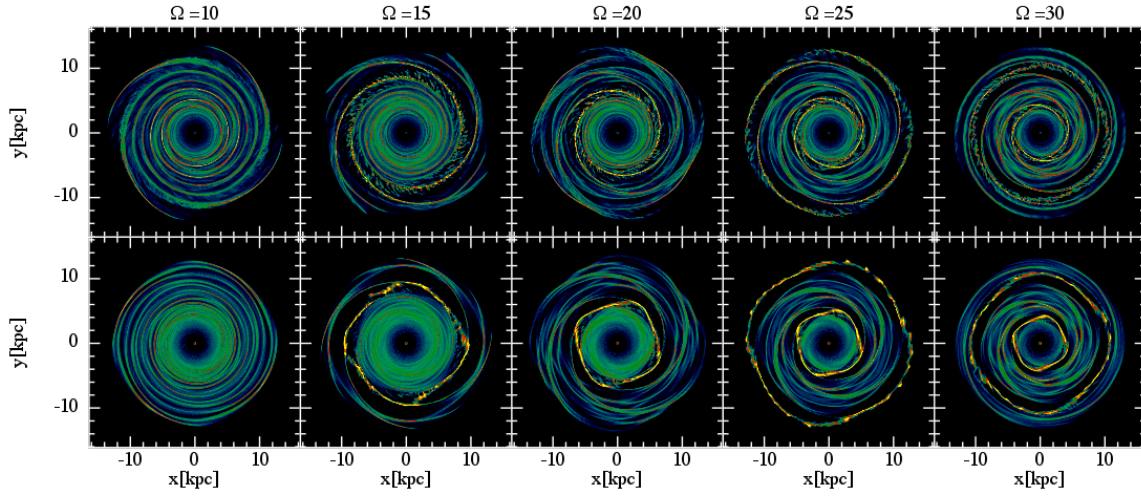


Figure 3.6: Isothermal simulations with $T = 200\text{K}$ and varying spiral arm pattern speed ($10\text{--}30\text{km s}^{-1}\text{ kpc}^{-1}$, increasing to right) for a four-armed potential at two different times (400 Myrs top and 1 Gyr bottom).

branches that are not associated with the bottom of the potential well. The increased temperature of the simulations with warm gas makes the gas much more diffuse, and disperses these features. Traces of these branches can still be seen, but are much less defined than the cooler simulations (seen by comparing the hot and cold $N = 4$ models). Shocks experienced upon the passage into arms are also much weaker. Another feature exclusive to the cold models is the onset of spurs (small scale features peeling away from the arms at a large pitch angle, see Dobbs & Bonnell 2006) in the mid-disc. These are clearest in the $N = 2$ case and occur near to the location of the ILR (see Fig. 3.1b).

To investigate the effect of the ILR and OLR on the gaseous structures further calculations were ran with differing arm numbers and pattern speeds, values of which determine the radial positions of the resonances. Figure 3.6 shows simulations with differing arm pattern speeds after 400 Myrs and 1 Gyr of evolution. As pattern speed increases to the right the location of the ILR can clearly be seen to radially contract, initially lying beyond the disc edge in the $10\text{km s}^{-1}\text{ kpc}^{-1}$ case. The OLR is then seen to appear as the pattern speed is increased, becoming apparent only in the model with the fastest rotation. The spurring appears predominantly at the ILR and OLR. At the later time stamp of 1 Gyr the gas at the ILR and OLR creates closed orbits that match the orbits proposed by density wave theory, the same as those shown in Figure 1.9. The spiral structure is then seen only to exist between the ILR and OLR. The timescales needed to see these enclosed orbits is well beyond the timescale required for chemistry to settle to a steady state (see Section 3.5). The location of these features can be used to infer some information about Galactic spiral structure. For instance, a $N = 6$, $\Omega_{sp} = 25\text{km s}^{-1}\text{ kpc}^{-1}$ model has an ILR inside of 10 kpc and therefore it is unlikely that such a model would produce spiral features beyond this radius, such as seen in the Outer arm, and so is a poor choice for our Galaxy.

There appears a lot of branching structure between the arms in the colder models, and this

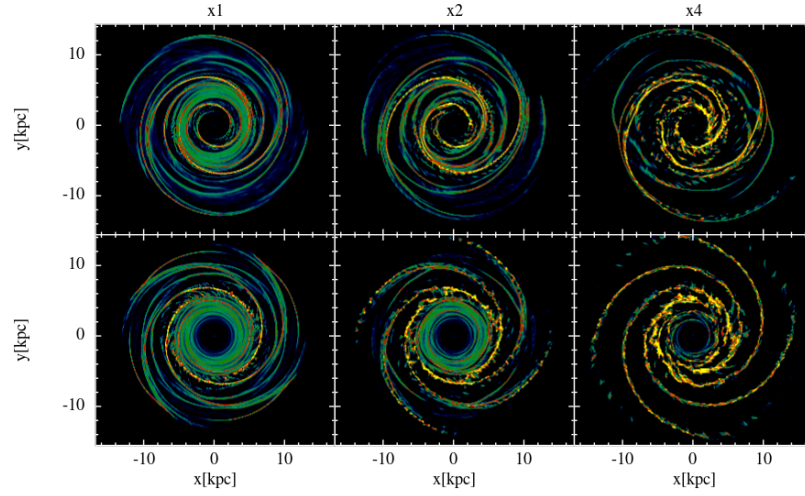


Figure 3.7: Isothermal simulations of with $T = 200\text{K}$ with varying potential strength ($1, 2, 4 \times \rho_0$) after 400 Myrs of evolution. The top and bottom rows show $N = 2$ and $N = 4$ models respectively.

is especially so in the case of $N = 2$. The superposition of arm features in the CG model could be a cause of this, due to the triple minima nature of a superimposed three component spiral pattern. To check this was not the case, calculations were performed with only certain components of the spiral summation in Equation 3.6 active. The resulting spiral structures were much weaker than in the three component case, and less pronounced at larger radii. Furthermore, the inter-arm branches were still present, implying they are not a result of the superposition nature of the CG model.

Some of the arm features are quite weak in the plots shown above, even between the ILR and OLR. To try and improve the tracing of the spiral potential in these models, calculations were performed with $\times 2$ and $\times 4$ the standard spiral arm density (ρ_0 in Equation 3.6). The results of 2 and 4 armed calculations with different strengths are shown in Figure 3.7. The higher the strength, the higher the densities in the arms become, and the clearer the spiral structure in the gas appears. The highest strength calculation has little gas in the inter-arm region, not merely just low density gas, but very few actual gas particles. There is also a significant amount of dispersion in the rotation curve in the highest strength calculation. There appears to be a sort of buckling effect near the ILR, where the highest density regions are not tracing the logarithmic spiral structure well. Due to these reasons the $\times 4$ strength model seems inappropriate for further use. However the $\times 2$ model still has a large amount of inter-arm gas and only moderate dispersion of the rotation curve, so this model is deemed as appropriate for further calculations with chemistry and cooling along with the fiducial value.

The bar models show a similar behaviour with pattern speed as the arm models. However, as they are believed to be rotating much faster than the arms, the OLR will usually lie within the inner Galactic disc. All bars have the same general features, and we will be using the WK and LM bars for further chemical and cooling calculations (we will discuss the morphology of these in greater detail later in this chapter).

The LM bar has been included to specifically allow the alteration semi-major and minor

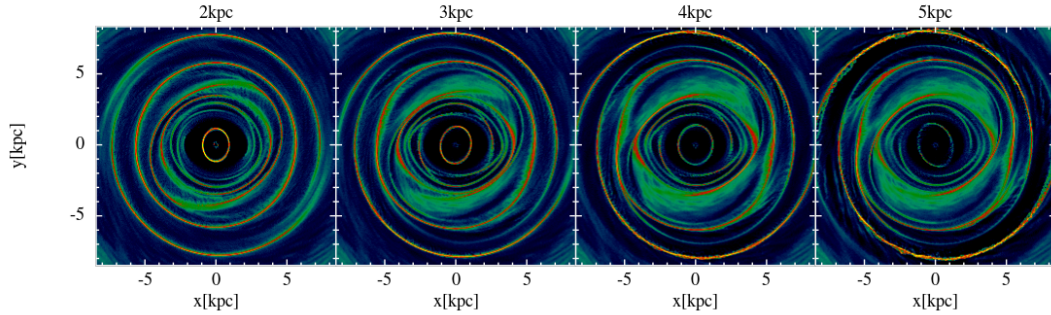


Figure 3.8: Isothermal disc simulations at $T = 200\text{K}$ with an LM rotating at $\Omega_{bar} = 50\text{km s}^{-1} \text{kpc}^{-1}$ with different bar lengths of 2, 3, 4, 5kpc increasing to right and an axis ratio of 4:1.

axes. Calculations with bar lengths of 2, 3, 4 and 5kpc are shown in Figure 3.8. It can be seen that the increase in major axis has a minimal effect on the gas morphology. The shortest bar has reduced arm-like features compared to the other arms, presumably simply because the bar does not span as large a radial distance of the Galactic disc. Likewise the bar driven arms appear slightly stronger the longer the bar becomes. The longer the bar becomes the greater the shearing off these structures becomes, similar to that seen in the arm potentials. Tests were conducted with different semi-major to semi-minor axis ratios, ranging from values of 2:1 to 6:1. As the semi-minor axis is decreased with respect to the major axis (i.e. the bar becomes narrower) the inner structures such as those seen in the 3kpc case in Figure 3.8 become more defined, but in doing so causes a larger dispersion in the rotation curve. Similar effects are seen in the study of Lee et al. (1999) who find that the gas infall to the Galactic centre increases as the bar axis ratio increases. Inner bar structures are weak when using a ratio of 2:1, whereas Rodriguez-Fernandez & Combes (2008) and López-Corredoira et al. (2005) find this as the nominal value, though they use a much more complex potential than that of LM. Changes are only minor when using sensible values such as 3:1-5:1 (Dwek et al. 1995; Freudenreich 1998) so 3:1 is adopted as our fiducial axis ratio for the LM bar.

Tests of the complex bar of Wang et al. (2012) showed there was in fact very little difference morphologically between this and the other bar models. The minor differences showed features were more in common with the WK than the LM model, which is somewhat surprising given differences in the potential fields shown in Fig. 3.2. Though in models where we included the bulge of Wang et al. (2012) rather than fiducial Plummer bulge there was a suppression of the inner elliptical structures. These structures are seen in other studies with complex bars also (Kim et al. 2012) and are also reproduced in our simulations with live stellar systems where bars are formed (see Chapter 5). Overall, a lack of difference in the global morphology lead to the excluding of this bar from further analysis in an attempt to narrow down our already considerably large parameter space.

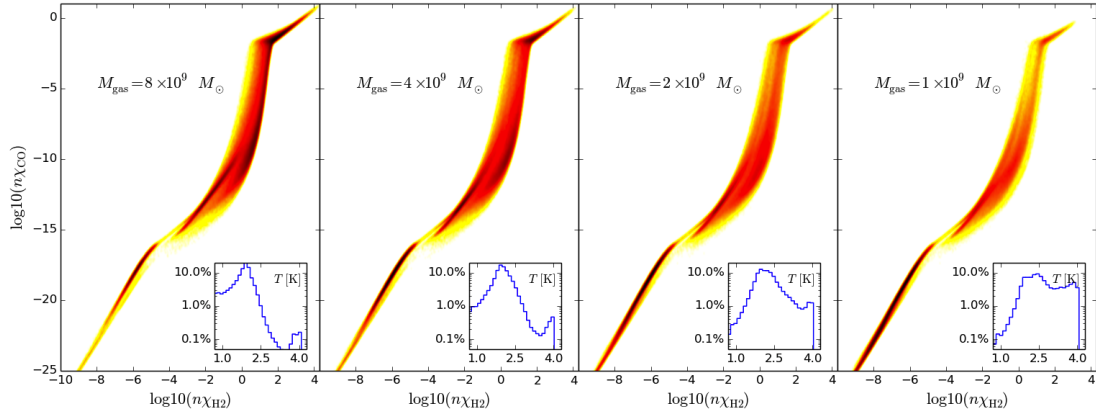


Figure 3.9: Abundance of molecular gases, weighted by density, in simulations with various surface densities (decreasing right to left). The temperature distribution for each surface density is shown in the insert in each panel. The higher the surface density runs have a greater mass of molecular gas.

3.5 General results of chemistry and cooling

Once a selection of appropriate potentials and parameters to be investigated had been narrowed down they can be used in simulations with active ISM chemistry and cooling to track the model the evolution of molecular gas for the construction of CO l - ν emission maps. These simulations take considerably longer to perform than say isothermal simulations at $T = 200\text{K}$, mostly due to the cooling time-step criterion controlled by Equation 2.41. Computational time is also increased due to the additional chemical sub-stepping that acts inside the cooling time-stepping, but as this does not involve updating the positions or velocities of the SPH particles it is relatively inexpensive.

The abundance of H_2 and CO as a function of particle density is shown in Figure 3.9 for a simple barred-spiral disc galaxy simulation of 1 million particles after 200 Myrs of evolution. The figure shows the abundances weighted by number density of the particle to disperse the region in the upper right where the carbon and hydrogen is nearly saturated into CO and H_2 . The particles perform move in molecular abundance-density space as they pass into and out of high density regions. The molecular fraction of each particle increases as it passes into the high density potential well of the arms/bar, and drops when it leaves (for an in-depth discussion see Dobbs et al. 2008). The higher the surface density (i.e. total gas mass) in the simulation then the more efficient it is at producing and maintaining molecular gas. The lowest surface density shown here has a very small amount of molecular gas, and also a very small cold ISM population, seen in the small histogram insert. Our fiducial surface density (far left panel) has a well populated cold ISM component where molecular gas is maintained ($T \approx 10\text{K}$), while also displaying a moderate warm component ($T \approx 100\text{K}$). The effect of surface density on the actual emission will be discussed in the next Chapter.

In Figure 3.10 the evolution of the molecular gas content over time is shown for the same simulations as in Fig. 3.9. The figure shows the H_2 ratio and CO abundance summed over all 1 million particles with different colours illustrating different surface densities. There is a rapid

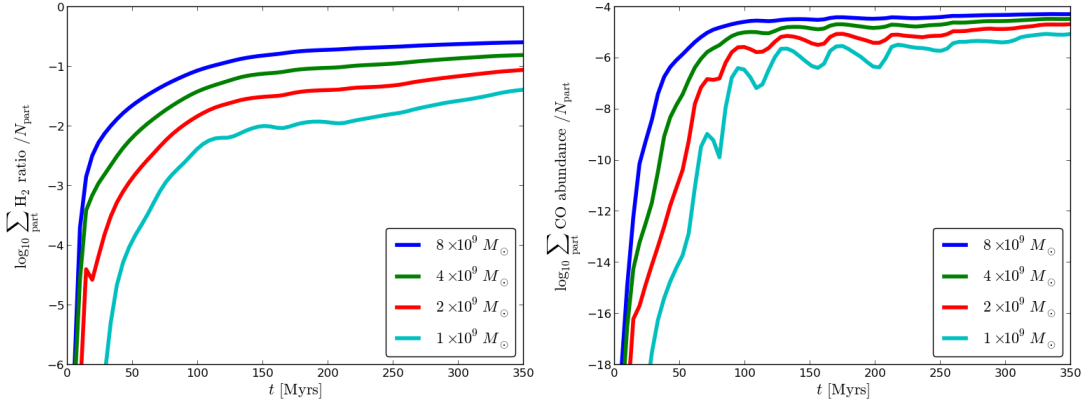


Figure 3.10: The time evolution of the molecular gas abundances averaged over all particles in a barred-spiral simulation with 1 millions SPH particles and various surface densities. H_2 and CO are shown to the right and left respectively. Large scale changes in the amount of molecular gas appears to cease after approximately 100Myrs.

increase in molecular content in the first 50 Myrs, which coincides with the time-scale for the spiral and bar patterns to become clearly visible in the gas density. The CO and H_2 evolution reaches a steady state plateau after approximately 100 Myrs, where changes of the order of magnitude no longer occur. Simulations with cooling and chemistry are chosen to run until at least 300 Myrs and until a maximum of 472 Myrs. This is the timescale needed for arm and bar structures to become well developed, but they will continue to slowly evolve on the order of Gyrs (Fig. 3.6). Despite the abundance sums being independent of gas mass/density there is a clear separation between runs with surface densities, showing that the higher surface density calculations are inherently more efficient at producing molecular gas, as expected. The evolution of CO abundance in the lowest mass calculation displays oscillations of an order of magnitude on a timescale of 40Myrs. This is assumed to be the result of gas in the lowest mass simulations being very susceptible to destruction, falling into the lower tracks in Fig. 3.9. The oscillation occurs as gas that was in the bottom of the potential well at $t = 0$ Myrs leaves at later times and experiences an abrupt loss of molecular gas. The peak is then reached by gas that is rising in density as it flows into the arms, but again drops abruptly as it leaves. This is less pronounced in higher mass calculations where the gas mass is higher and higher density gas is well shielded against abrupt molecular destruction due to the higher column densities.

The gas properties in our simulations as a result of the cooling and chemical effects are similar to those seen in the phase diagrams of Figure 2.12. We find that there is a significant amount of gas found within the thermally “unstable” regime, with temperatures of the order of 100K to 1000K. The amount of this unstable gas is a strong function of surface density (i.e. total gas mass) used in the simulation, seen in the temperature histogram inserts in Figure 3.9. These histograms also clearly show a two-peaked distribution at temperatures of 10^2 K and 10^4 K, which correspond to the warm and cold ISM components. The lower the surface density, the larger the warm gas fraction, and lower the cold gas fraction. For example, in the highest and lowest surface density calculations the warm component ($6000\text{K} < T < 10000\text{K}$, as defined in Table 1.1)

constitutes 1% and 10% of the gas mass respectively, while the cold component ($50 < T < 100\text{K}$) takes up approximately 45% and 17% respectively. These values are similar to those of Dobbs et al. (2008) but with slightly different definitions of warm and cold components. The rest of the gas is composed of gas transitioning between the phases in the unstable region, or is locked in a very cold molecular component, especially so in the heaviest gas disc. Having a large amount of supposedly unstable gas which has been seen in observations (Heiles & Troland 2003) and previous numerical simulations (Kritsuk & Norman 2002; Piontek & Ostriker 2005; de Avillez & Breitschwerdt 2004). The amount of molecular gas produced is also a strong function of surface density, as it is well shielded in the high density regions found in cold pockets of the ISM. The molecular mass fraction is dominated by the H_2 , with CO being 3 or 4 orders of magnitude lower. The highest mass disc has a molecular mass fraction of approximately 4.0% (out of a total mass of $8 \times 10^9 M_\odot$), while the lowest surface density disc has a value of 0.5% (out of $1 \times 10^9 M_\odot$). While our standard surface density may seem appear too high, in that it produces a low amount of warm atomic gas, we show in Section 4.4 that the higher surface densities are required to create sufficient CO emission to be on the same scale as those seen in observations.

3.6 Simple kinematic l - v maps

When building synthetic l - v maps to constrain Galactic structure there is another substantial parameter space that needs to be explored in addition to that parameterising the morphology of the potentials. The co-ordinates of the observer, i.e. the velocity, radial and azimuthal position (V_{obs} , R_{obs} and l_{obs}), adopted have a direct impact on the features seen in l - v space. A shift in an observers position of only 0.5 kpc could make the difference between a spiral arm lying in the inner or outer galaxy, completely altering its position in l - v space. The azimuthal position of the Earth in the Galactic disc has a similar effect, with changes in this value shifting structures in longitude, an effect that is more pronounced the closer these structures are to the Solar position.

The International Astronomical Union (IAU) recommends values for V_{obs} and R_{obs} of 220 km s^{-1} and 8.5 kpc respectively, but there are a wealth of other values used in the literature (see Reid 1993 and Majewski 2008 and references therein). l_{obs} is less well defined, as it encompasses both the distance from the Earth to arms and the orientation of the bar, while in our calculations it is simply a co-ordinate to be defined. Rather than simply assuming some standard value, each simulated CO l - v map was fitted to the observed CO map to find a best fit V_{obs} , l_{obs} and R_{obs} for the calculation in question. In order to fully explore the observer parameter space we would need to construct numerous l - v maps. If we were to construct full radiative transfer maps (as done in Chapter 4) for each point in the observer parameter space then the computational cost would be extremely high as this would have to be done for each model, at each time step of interest. We instead use approximate l - v maps to fit to the observers position, rather than performing radiative transfer calculations for each case. By doing so the computational time is reduced from the order of a day to seconds to build a single CO l - v plot, allowing a fast sweep through observer co-ordinates. Once the best-fit observer position is known for a specific galactic simulation we then perform a full radiative transfer calculation with `TORUS` to construct a map that is used for

comparing different spiral/bar models.

These purely chemo-kinematically derived maps are a simplification compared to those constructed with TORUS, but give a good idea of the position of the emission in l - v space, and a rough idea of its intensity. The maps are constructed as follows. First we choose the observer co-ordinates from the grid of observer parameter space (V_{obs} , l_{obs} and R_{obs} , with ranges given in Table 3.2). Then we calculate a synthetic CO brightness temperature, $T_{B,\text{synth}}$, from each SPH particle in the simulation using the particle's velocity, position and CO abundance. As the CO is heavily density dependent, this contains density information for each particle. To create a quantity analogous to emission we use a simple radiative scaling law of the form

$$I_{i,\text{synth}} \propto \chi_{i,\text{CO}}/d_i^m \quad (3.18)$$

where $\chi_{i,\text{CO}}$ is the abundance of CO for the i^{th} SPH particle and d_i is the distance from the observer to the particle. This is similar to the approach of Dobbs & Burkert (2012), except we do not need to assume the density profile of the ISM gas as it is provided by the SPH particles in the abundance of CO. While the brightness temperature does not technically follow an inverse square law, the column density (and therefore opacity) of material the emission passes through does increase with distance. The I_{synth} factor is then scaled for each particle to match the range of emission in the observed CO map, giving a value of $T_{B,\text{synth}}$ for each particle.

A longitude velocity map is then constructed using the SPH particle coordinates and assuming the observer is on a purely circular orbit. The particles are all first rotated by l_{obs} and then their line-of-sight velocity is calculated as given in Binney & Tremaine (1987);

$$v_{\text{los},i} = \sqrt{v_{x,i}^2 + v_{y,i}^2} \sin(l_i - \theta_{v,i}) - V_{\text{obs}} \sin(l_i), \quad (3.19)$$

where simple geometry gives the longitude of the particles, $l_i = \arctan(y_i - y_{R_o}/x_i - x_{R_o})$ and the velocity vector is at an angle of $\theta_{v,i} = \arctan(v_{y,i}/v_{x,i})$. An extra b factor for latitude dependence can also be included but it made no difference to the quality of the fit, likely because our simulations vary little in the vertical direction. There is evidence that the Sun exhibits peculiar motion relative to the local standard of rest of the order 10 km s^{-1} (Dehnen & Binney 1998). We investigated adding peculiar motion (up to 20 km s^{-1}) for a single model and the resulting best fitting map showed little difference to the case of a circular orbit. For the remainder of this thesis we assume circular orbits to reduce our parameter space.

The emission (in log-brightness temperature) of the particles is then binned into a grid of l - v space of the same resolution as the Dame et al. (2001) CO map (0.125° by 1 km s^{-1}). Particles act as a point source, with emission occupying a single pixel of l - v space. To better represent the structure of ISM observations the emission from each particle is broadened and smoothed out into neighbouring l - v bins. The value of this smoothing, and the exponent in Equation 3.18, are parameters that must be set to build an l - v map. To do so the maps cannot be fit against the observed l - v map, as this would assume the model is a correct representation of Galactic structure. Instead these kinematic l - v maps were compared to ones created using the TORUS radiative transfer code, which will be used to create full synthetic observations and is the subject of the following Chapter.

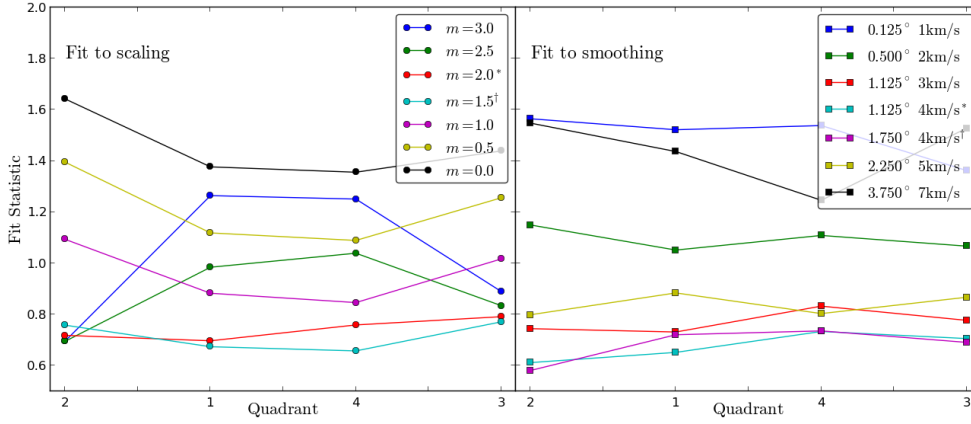


Figure 3.11: Fit statistic as a function of differing powers in distance drop-off (m in Equation 3.18) in the left panel and as a function of smoothing in longitude in the right, across the four Galactic quadrants.

Best fit values of the smoothing and scaling were found by minimising the difference between the kinematic and TORUS maps, using a simple mean-absolute-error statistic. The behaviour of the fit as a function of these parameters is shown in Figure 3.11, across all four Galactic quadrants. In the left panel the fit to m is shown, and on the right the fit to the longitudinal smoothing, with the two best fitting values given a * and † in the legends. The figure shows the best fitting values lie in the range $m = 1.5$ -2 and $dl = 1.125^\circ$ - 1.725° , surprisingly showing the emission can indeed be approximated by a inverse square law. This longitudinal smoothing is somewhat larger than that of the binning of the Dame map, but is required to smooth out the point-like SPH particles into a finite size (a further improvement to this method would be to use the SPH smoothing kernel to give each particle a physical size). The adopted values for smoothing are a half width of 1.125° in longitude and 4 km s^{-1} in velocity using a Gaussian profile, with a $m = 2$ decay. The 4 km s^{-1} velocity smoothing matches the turbulent velocity width we add to the TORUS maps (discussed in Chapter 4). The smaller of the smoothing scales was chosen as the maps made using $dl = 1.725^\circ$ seemed to be over-smoothed when viewed by-eye.

Figure 3.12 shows l - v maps constructed within a barred galaxy simulation. The upper panel shows a map made using the method described above, and the lower panel shows a map made using the radiative transfer technique. Both are constructed using the same values for V_{obs} , R_{obs} and l_{obs} . Both maps trace the same regions of l - v space, with roughly the same intensities. The simple map underestimates the emission in some regions, and overestimates in others. This is expected; if the simple map reproduced the TORUS map there would be no need to perform the radiative transfer calculation.

These simple maps enable us to find a best-fitting map for each individual Galactic simulation, removing the uncertainty in placing the observer at some arbitrary position. The range of observer co-ordinates investigated in this fit are given in Table 3.2. Once a best fit is known, TORUS is then used to build a full map using the best-fitting observer co-ordinates, which can then be used to compare the different galactic potentials.

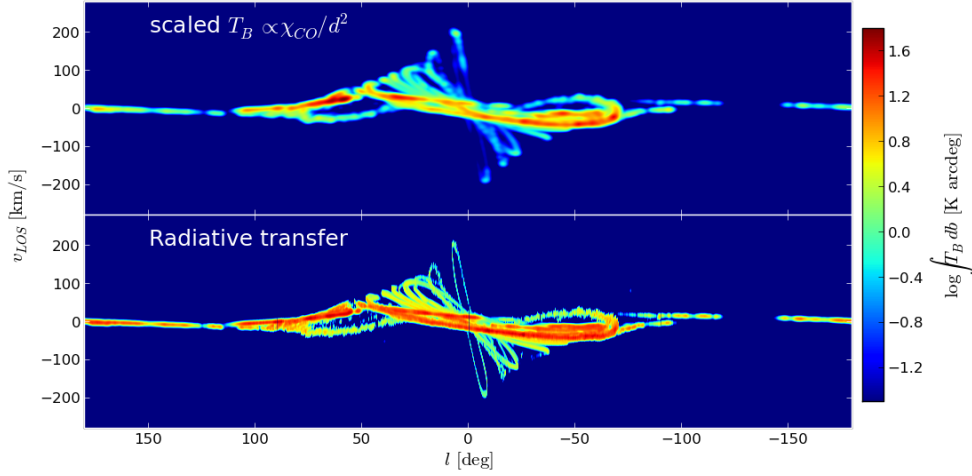


Figure 3.12: Two emission maps of a barred Milky Way simulation, of WK type. Top: synthetic CO l - v map constructed using Equation 3.18. Bottom: l - v map created at the same observer coordinates but with the radiative transfer code TORUS, with the same values of R_{obs} , V_{obs} and l_{obs} .

To quantify the goodness of fit for each model we use a simple fit statistic. We calculate a mean absolute error (MAE) to gauge the goodness of fit. Our choice of MAE over RMS is to ensure that single pixels far from the observed value do not cause severe deterioration in the fit statistic, as we are interested in a global match, rather than whether individual features can be exactly reproduced. The emission is first integrated in latitude and then the logarithmic difference, $\log T_B db$, is compared between the synthetic map and the CO map of Dame et al. (2001). This is then normalised by the number of pixels with non-negligible emission in the observed l - v map, n_{pixels} , simply to obtain a fit statistic close to unity (this is the same value for all maps). The form of our fit statistic is thus,

$$\text{Fit} = \frac{\sum_{\text{pixels}} |\log T_{B,\text{synth}} db - \log T_{B,\text{Dame}} db|}{n_{\text{pixels,Dame}}}, \quad (3.20)$$

where $T_B db$ is the brightness temperature integrated over latitude. This is therefore the sum of the logarithmic ratio of the integrated synthetic brightness temperature to the observed brightness temperature for a specific longitude-velocity bin. Initially a linear summation was used, but the fit had a great tendency to be swayed by a single pocket of strongly emitting dense gas that did not agree with observations. We effectively calculate the linear deviation from the emission features shown in maps such as Fig. 3.12, where the intensity is shown on a log scale to highlight low lying features. Note that due to the non-zero nature of the background emission in the observations (which is also added to the synthetic map) there is never a case when a divide by zero occurs in the logarithm, or where $\log 0$ occurs. This statistic was tested using a simple model 4-armed model against the Dame map and varying the azimuthal position of the observer. The fit statistic was then measured in individual quadrants to check the desired behaviour; that the minimum was seen when arm features aligned with those seen in observations. This was easiest done in the second

and third quadrants where the Perseus and Carina arms are clearly visible. The use of this fit statistic blindly however is somewhat dangerous, as a model that is a seemingly good fit but has arm features that are only slightly misplaced in velocity space will have a poor fit statistic, despite having the arms in a near perfect position. The variation of the observers position rectifies this somewhat, allowing for the movement of l - v features for each model. However, as in fitting we still must produce l - v maps to compare to observations, we double check by-eye that no seemingly good model has been discarded for having a poor fit despite it showing a relatively good match. In actuality this only occurred on a few cases, once for a barred simulation, which was not better than those of other potentials anyway, and one for a live-disc calculation (which is discussed in Chapter 5). Because our simple approximate l - v maps and those made using radiative transfer are calculated using two very different methods the fit statistic should not be quantitatively compared between these two different types of map. However, the relative strength of emission features, and the general morphology, can be.

Now a parameter space, model prescription, mapping methodology and quantitative fit statistic has been established we can now move on to exploring the morphological parameters with high resolution calculations. Sections 3.7 and 3.8 describe simulations with bar and arm potentials respectively, where the effect of pattern speed and morphological parameters upon l - v features is investigated. This is used to narrow down the parameter space for the next Chapter, where we will conduct simulations with both arm and bar potentials, and produce l - v maps using full radiative transfer rather than the simple prescription outlined above. A key caveat to this approach is the assumption that a bar/arm model that provides a good fit in isolation will do so when combined with another potential. While this may not be necessarily correct, it allows for an approach with a realistic amount of free-parameters. This is not an entirely unfounded assumption, as the bar and arms will dominate the gas morphology in the inner and outer galaxy respectively, with only the region of $4 < R < 7$ kpc being influenced by both (seen from inspection of the isothermal simulations in the previous section).

3.7 Barred simulations with cooling and chemistry

3.7.1 Simulations

An example of the evolution of a barred galaxy simulation with active chemistry and cooling is shown in Figure 3.13, using the bar model of Wada & Koda (2001) with a core radius of 2 kpc rotating at $50 \text{ km s}^{-1} \text{ kpc}^{-1}$. When using different bar potentials the overall evolution is similar. The bar potential is active throughout the entire simulation, and gas within the bar establishes elliptical orbits along the major axis of the bar from 100 Myrs onwards. After 150 Myrs the gas in the outer disc displays a two armed spiral structure inside the OLR, the strength of which is related to the core radius and strength of the potential. These arms are not in a steady state, and their pitch angle is decreasing over time. After about 4 rotations of the bar (the last panel in Fig. 3.13) the arms are wound up enough that they begin to join to create elliptical/ring-like structures at the OLR, with the orbits set as being either perpendicular to the bar inside the OLR or parallel to outside the OLR (Combes et al. 1995; Buta & Combes 1996; Mel'Nik & Rautiainen 2009). Any

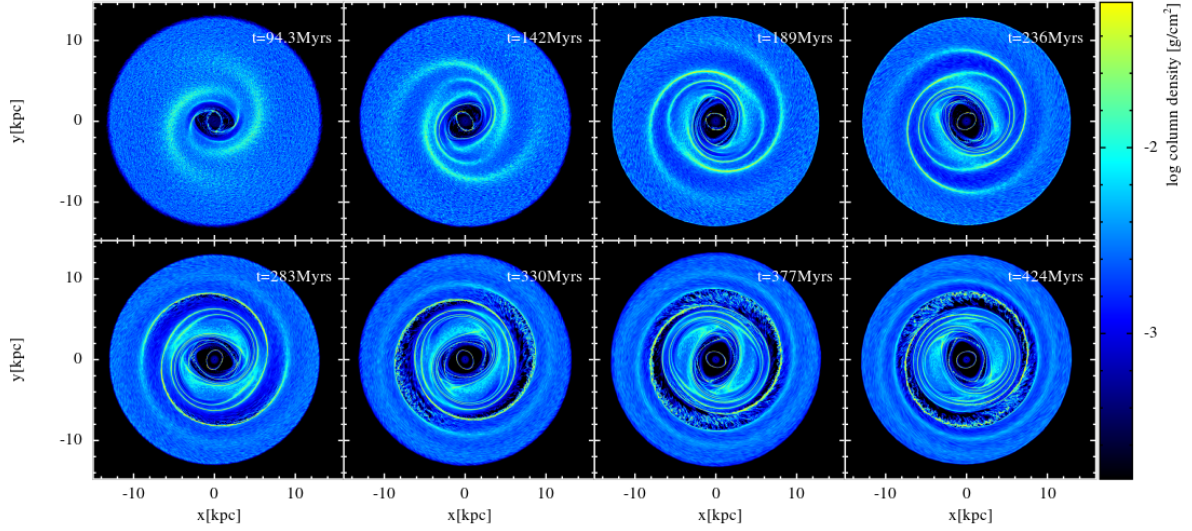


Figure 3.13: The evolution of the bar model of Wada & Koda (2001) with a core radius of 2 kpc rotating at $50 \text{ km s}^{-1} \text{ kpc}^{-1}$. Both the bar and the gas are rotating clockwise. Note that the morphology is effectively the same from 350-470 Myrs and the arms will eventually wind up to form a ring-like structures with elliptical orbits parallel and perpendicular to the bar major-axis. The orientation of the features in this and other top-down figures is determined by the initial alignment of the non-axisymmetric potential with the x-axis at $t = 0 \text{ Myrs}$, orientation does not correspond with any of the l - v maps shown in other figures.

arm potential we combine with these bars would be substantially subdued in this region, which is near to the Solar radius. At early times there is a distinct sweeping up of gas inside the ILR, seen in the earliest three panels. In the low density region around $R = 2 \text{ kpc}$ at later times there are very few SPH particles, as most are now associated with the inner ring or the outer region. In the case of Figure 3.13 there is significant infall of gas onto the central, bar dominated, region but this seems to cease after approximately 150 Myrs. This may indicate the end of the bar infall phase, or merely be a resolution effect and there are simply no more free particles within the capture distance of the inner bar. In Figure 3.14 the surface density for several models is shown as a function of radius. The left panel shows the initial profile, and that of an armed, barred, and barred-spiral calculation after 236 Myrs of evolution. The surface density is effectively unchanged in the armed model, but there is a significant infall of gas into $R < 2 \text{ kpc}$ in models with a barred potential, at the expense of gas inside $R < 3 \text{ kpc}$. In the right panel the evolution of a barred model is shown, which indicates the infall phase ceases after approximately 170 Myrs. Over this time gas from $1 < R < 3 \text{ kpc}$ falls into the rings around $R = 1 \text{ kpc}$.

In test calculations where we use an isothermal equation of state to model the ISM the arms driven by the bar are maintained when the temperature is high (10000K). However, in low temperature isothermal cases and adiabatic+cooling cases the arms enclose on the aforementioned set of orbits around the OLR. There also exists a set of orbits perpendicular to the bar in the inner galaxy. These orbits (commonly referred to as x_2 orbits) only exist when there is a region between two separate ILR's (Contopoulos & Papayannopoulos 1980). In calculations where we used a

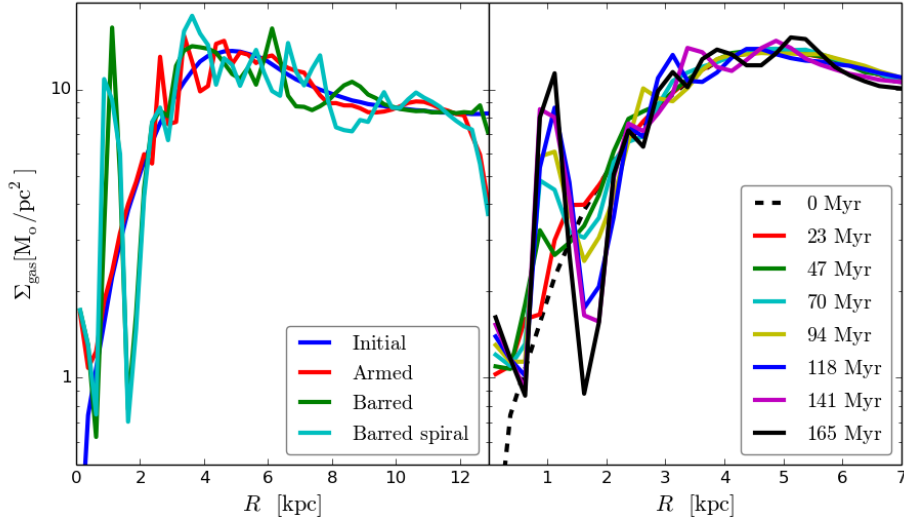


Figure 3.14: The gas surface density profile as a function of R for three different models after 236 Myrs of evolution (left) and time evolution for a barred calculation (right) showing gas infall occurs in barred models within $R < 3$ kpc up to 170 Myrs.

more simplified axisymmetric potential (a bulge-less flat logarithmic potential) there were no such inner orbits as there was only a single ILR. However the rotation curve we use here has an inner bulge (see Fig. 3.1b), providing a second ILR and so setting up a family of inner perpendicular orbits. These orbits are seen in other works using analytic barred potentials (e.g. Lee et al. 1999; Mel’Nik & Rautiainen 2009). When using the LM bar model these inner orbits contract radially as the semi-major or semi-minor axis is decreased (Fig. 3.8).

The pattern speed of the bar is key in determining the structures that develop in the inner Galaxy. Plots of the WK bar model are shown at various pattern speeds in Fig. 3.15. All the bar potentials used in this study display similar behaviour as a function of pattern speed. As the pattern speed increases, the ILR and OLR contract, reducing the radial extent of features driven by the bar. There is also an inability of the slower bars to drive any strong arm-like features compared to the faster pattern speeds, owing to the fact that the OLR is beyond the edge of the Galactic disc. The slower bars also have a greater impact on the dispersion in the rotation curve compared to the faster bars. The $20 \text{ km s}^{-1} \text{ kpc}^{-1}$ bar in Fig. 3.15 has a dispersion of around $\pm 50 \text{ km s}^{-1}$ at $R = 2 \text{ kpc}$. Conversely the faster bars have a greater variation in the rotation curve in the outer regions of the disc corresponding to the location of the driven arms, but of a much smaller scale than that of the inner region of the slow bar.

Figure 3.16 shows a comparison between our three different bar models. All have a pattern speed of $50 \text{ km s}^{-1} \text{ kpc}^{-1}$ and are shown after 236 Myrs of evolution angled at 45° with respect to the Sun-Galactic centre line. The inner x_2 orbital structure is similar for all models. Immediately outside this there are other thin orbital structures, more so in the case of the LM bar. The arm structures generated in the outer disc are different in each model. The LM bar has formed very tightly wound arms compared to the others, a result of the different radial drop-off compared to the other models. The LM bar potential is thinner along the semi-minor axis than the others, which

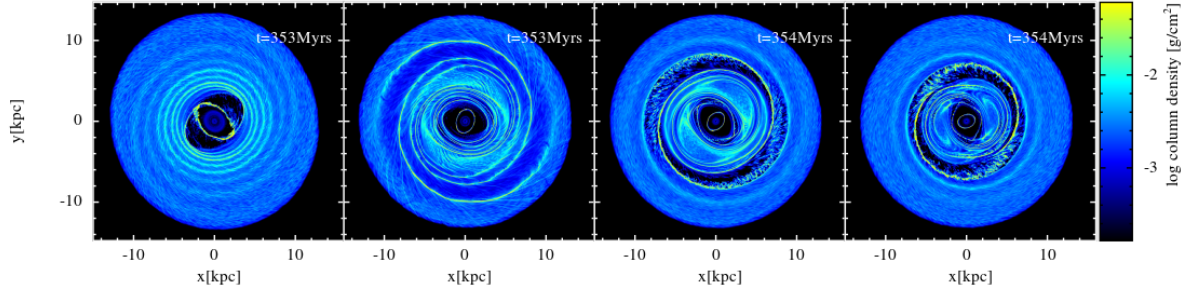


Figure 3.15: The bar model of Wada & Koda (2001) with a core radius of 2 kpc rotating at pattern speeds of 20, 40, 50 and 60 $\text{km s}^{-1} \text{kpc}^{-1}$, increasing from left to right, at a time of 354 Myrs. The gas and potentials are rotating clockwise viewed from above. These top-down maps correspond to the central row of Fig. 3.18. The contraction of the outer Linblad resonance is clearly as $\Omega_b = 50 \rightarrow 60 \text{km s}^{-1} \text{kpc}^{-1}$. The 70 $\text{km s}^{-1} \text{kpc}^{-1}$ model is not shown but is similar to the 60 $\text{km s}^{-1} \text{kpc}^{-1}$ model but with bar/arm features confined to $R < 6 \text{kpc}$.

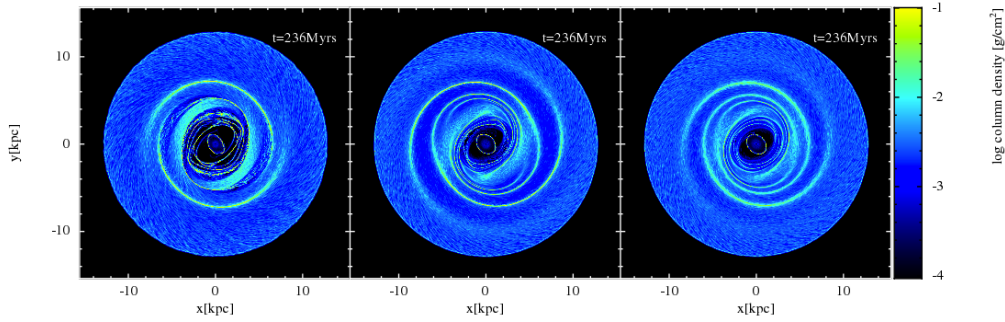


Figure 3.16: Different bar models angled at 45° to the Sun-Galactic centre line with a pattern speed of $50 \text{km s}^{-1} \text{kpc}^{-1}$ after 236 Myrs of evolution. The models (left to right); WK, WKr2 and LM are described in the main text.

could also contribute to the tighter arm structures. The WK and WKr2 bars differ in the extent of their central core radius, the effect of which can be seen in Fig. 3.16. The bar with the smaller core radius has weaker arms compared to the bar with a larger core.

3.7.2 Simple kinematic maps

Results for a single bar model

Fitting to the observers co-ordinates was then performed on the chemically/cooling active simulations described above, using the WK, WKr2 and LM models, with the fit statistic of Equation 3.20 used to quantify how well each model reproduced the observed emission features. An example of the results of fitting to the observer’s co-ordinates is shown in Figure 3.17. The Galaxy model used in this example is a WK barred potential with a bar pattern speed of $50 \text{km s}^{-1} \text{kpc}^{-1}$. The parameter sweep is performed at a timestamp of 470 Myrs and the bar major-axis lies along the y-axis by default. The left panel of Fig. 3.17 shows that a best fit orientation of $\theta_b = 40^\circ$ is preferred, broadly in keeping within the accepted range for the “Long bar”. The fit as a function of velocity gives the IAU standard value of 220km s^{-1} , but it is clear the velocity fit is not as well constrained

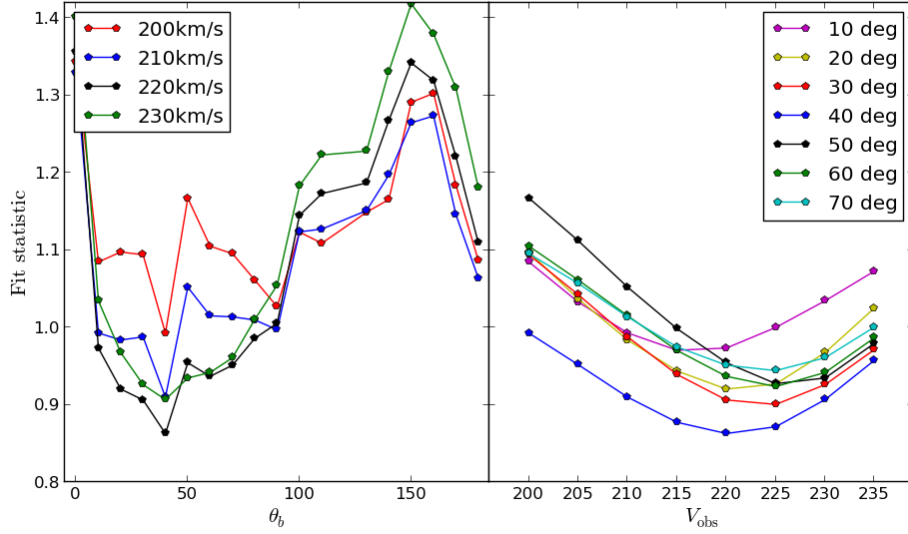


Figure 3.17: An example of fitting to the observer’s co-ordinates using simplified l - v maps as described in Section 3.6. Here we show the fit statistic for a barred Milky Way after 470 Myrs of evolution. The fits to the observers azimuthal position and circular velocity are shown in the left and right panels respectively at $R_{\text{obs}} = 8.5$ kpc (the fit as a function of R_{obs} is not shown for clarity). The different coloured lines show the fit for a certain value of V_{obs} (left) or θ_b (right).

as the bar orientation. While not shown here, R_{obs} is similar to V_{obs} in that it shows a shallow global minimum. This is the case with most potential models, with the l_{obs} parameter showing the clearest troughs/peaks of the fit statistic. The l_{obs} parameter is only shown between 0 - 180° , as the potentials, and fit statistic, are symmetric. While the azimuthal position of arm models in the literature seems poorly constrained, there is effectively no observational evidence for the bar major axis to not be pointing towards the second quadrant. That is to say, the bar orientation is always found to be $0^\circ < \theta_b < 90^\circ$, seen both in numerical (Weiner & Sellwood 1999; Yang et al. 2002; Minchev et al. 2007; Rodriguez-Fernandez & Combes 2008; Mel’Nik & Rautiainen 2009) and observational studies (Dwek et al. 1995; Binney et al. 1997; Hammersley et al. 2000; López-Corredoira et al. 2007) regardless of whether with respect to the *COBE* or “Long” bar. In some instances the best fitting bar orientation is found to be outside of this range. This occurs for about 10% of the models, across different potentials, strengths, pattern speeds, and time-stamps. In these instances there is a second minima that does place the end of the bar in the second quadrant. Here we allow for the slight influence of observational evidence and choose to only accept best fits that place the bar end in the quadrant heavily suggested by observations, choosing to orientation minima only in the range $0^\circ < \theta_b < 90^\circ$.

The resulting best fit l - v maps, from the fit to all bar parameters (Ω_b , θ_b , R_{obs} and V_{obs}) for the simulations in Fig. 3.15 are shown in Figure 3.18. Fig. 3.18 shows the best fitting l - v plots for pattern speeds of 20, 40, 50, 60 and 70 $\text{km s}^{-1} \text{kpc}^{-1}$ after 236, 354 and 472 Myrs of evolution. The parameters for each of the best fitting maps (θ_b , R_{obs} and V_{obs}) are over-plotted onto each individual map, along with the corresponding fit statistic. We do not show the maps of the WKr2 and LM bars but will include their quantitative results across all parameters later in this section. Inspection of

Figure 3.18 shows that bars moving at $50\text{-}70\text{km s}^{-1}\text{ kpc}^{-1}$ tend to favour an orientation of around 50° , while the lower pattern speeds favour lower values. This is a result of the shift in the OLR from the external Galaxy to the internal Galaxy as we increase pattern speeds, and the resulting location of the arms driven by the bar. For lower pattern speeds the arms extend to outside the Solar radius, up to the OLR. This means these arms fit the outer quadrants, while the central bar structure fits the inner quadrants. For the higher pattern speeds the driven arm structures lie inside the Solar radius, and so the bar and arm structure is contained within the inner Galactic quadrants alone, leaving the outer quadrants empty. The resulting two different bar pattern speed domains cause the different bar orientation ranges. Our grid of values for the θ_b parameter is fairly coarse, incrementing in steps of 10° from the bar's position at times of 236, 354 and 472 Myrs after being initially aligned with the x-axis at $t = 0\text{Myrs}$. As such there is an uncertainty up to 10° in the values given here. This means that the frequently used value suggested for the ‘‘Long bar’’ by Churchwell et al. 2009 of $\theta_b = 45^\circ$, is within the bounds of the values found here by our best fitting bars with $\Omega_b = 50\text{-}60\text{km s}^{-1}\text{ kpc}^{-1}$.

The l - v maps shown in Figure 3.18 rarely generate considerable structure in the outer quadrants. The exception is the $40\text{km s}^{-1}\text{ kpc}^{-1}$ model at later times, where the arm structures driven by the bar persist into the outer disc due to the OLR's position beyond the Solar radius. At later times the arm structures driven by the bar join to create closed orbits, that are clearly visible in the l - v diagram (especially for the $\Omega_b = 70\text{km s}^{-1}\text{ kpc}^{-1}$ cases). This process can occur on the Gyr time-scale, and could be a plausible progenitor of Galactic ring structures (Mel'Nik & Rautiainen 2009). While not shown here, the l - v maps of the WKr2 bar are very similar morphologically.

The best fitting structures fit one of two regions well. The first category of good fitting maps are those that simply fill out more structure in l - v space, such as the $50\text{km s}^{-1}\text{ kpc}^{-1}$ WK bar at 472 Myrs (bottom central panel of Fig. 3.18). In these cases the arms driven by the bar extend to relatively large radii, spreading the emission into a larger range of $|l|$. The other category of good fits are those where the strength of the emission in the inner Galaxy follows a pattern similar to the observed CO map. This ridge of CO emission not present in HI is often attributed to a molecular ring-like structure, but could also be explained by arm or bar features of the correct geometry (Dame et al. 2001, Dobbs & Burkert 2012). In Fig. 3.18 at early times, the $60\text{km s}^{-1}\text{ kpc}^{-1}$ bar is a good fit for central emission due to arm-like structures extending to a radius of about 5 kpc, with a fairly wide pitch angle. By 472 Myrs the arms have closed upon each other, creating an elliptical structure where the arms once were. Both early and late times fill out the same area of l - v space, but the advantages of an arm structure over that from a ring is that it can curve in the correct direction in l - v space. A elliptical or ring like structure would show 2-fold rotational symmetry about $l = 0^\circ$, $v_{los} = 0\text{ km s}^{-1}$, not seen in the observed CO l - v map. The strong central ridge is seen in the $20\text{km s}^{-1}\text{ kpc}^{-1}$ l - v maps in Fig. 3.18 seems to provide a reasonable match for the central ridge in the CO data. This structure actually results from the concentric rings surrounding the bar, as seen in Fig. 3.15. The addition of an arm potential disrupts these relatively weak structures easily, and are needed to drive outer arm features absent in the $20\text{km s}^{-1}\text{ kpc}^{-1}$ bar. The emission for this bar is also relatively confined to this ridge, in comparison to the early time 60 or $70\text{km s}^{-1}\text{ kpc}^{-1}$ maps.

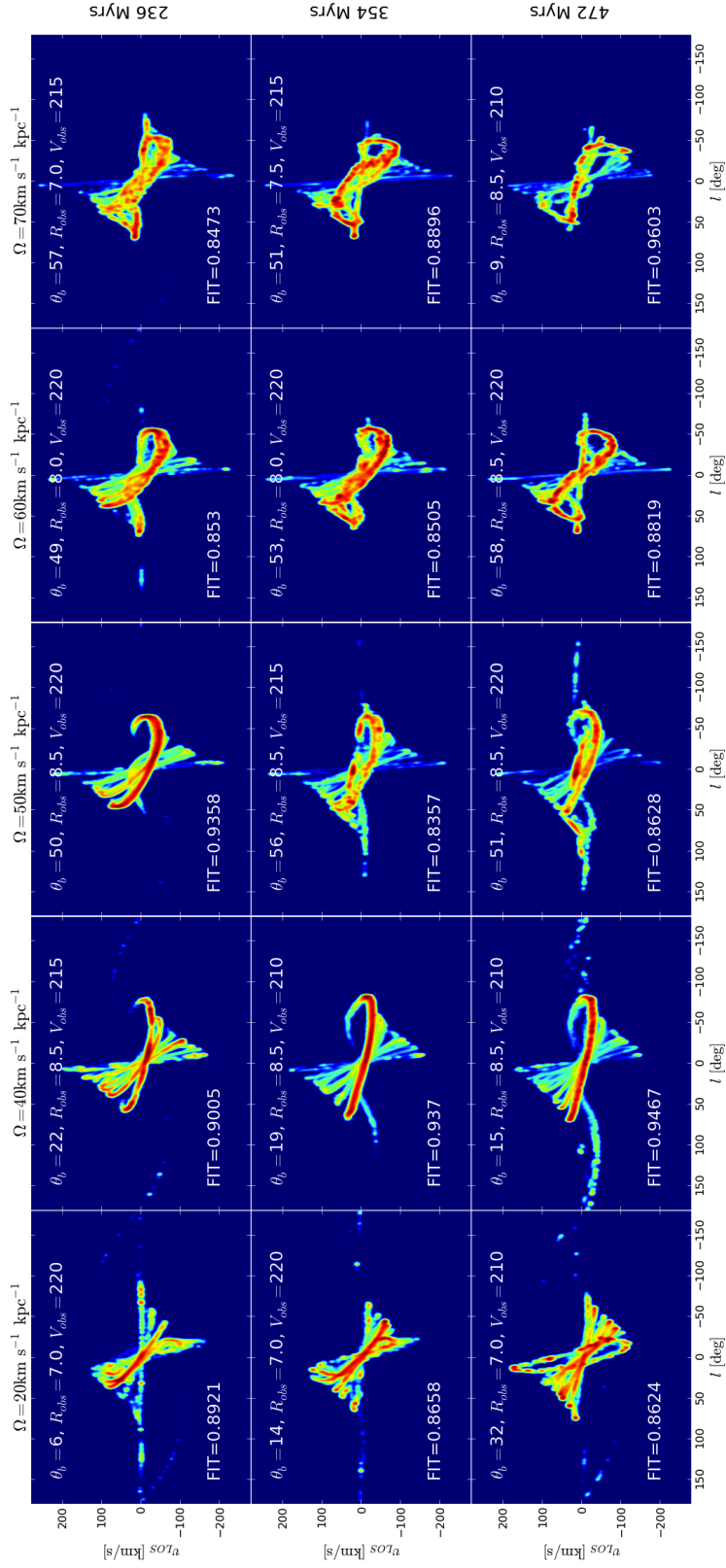


Figure 3.18: The bar model of Wada & Koda (2001) with a core radius of 2 kpc rotating at pattern speeds of 20, 40, 50, 60 and 70 km s⁻¹ kpc⁻¹ increasing from left to right with time increasing from top to bottom (236, 354, 472 Myrs). The values for the bar orientation, observer distance and circular velocity, and fit statistic are over-plotted on each Ω_b - l pair (in degrees, kpc and km s⁻¹ respectively).

Best fit parameter	Bar model		
	WK	WKR2	LM
Ω_b [$\text{km s}^{-1} \text{kpc}^{-1}$]	50	60	70
V_{obs} [km s^{-1}]	215	220	235
R_{obs} [kpc]	8.5	8.5	7.0
θ_b [$^\circ$]	56	51	41

Table 3.3: Best fitting values for the bar only simulations. A systematic uncertainty for each value is present due to the coarseness of the parameter space; $\Delta\Omega_b = 10\text{km s}^{-1} \text{kpc}^{-1}$, $\Delta V_{\text{obs}} = 5 \text{km s}^{-1}$, $\Delta R_{\text{obs}} = 0.5\text{kpc}$ and $\Delta\theta_b = 10^\circ$.

The l - v maps in Fig. 3.18 seem to be heavily time-dependent. Over a 200 Myr time frame the emission structures can change considerably. The $60\text{km s}^{-1} \text{kpc}^{-1}$ model in particular changes from having an emission ridge comparable to observations to a looped structure that is a poor by-eye match to the CO data. Maps of the WKr2 bar (a smaller core radius) evolve slower than the WK bar, maintaining their features due to the relatively weaker potential. For example the $60\text{km s}^{-1} \text{kpc}^{-1}$ map at 472 Myrs does not display the strong figure-of-eight like structure seen in the equivalent map of the WK bar (Fig. 3.18).

Results across all bar models

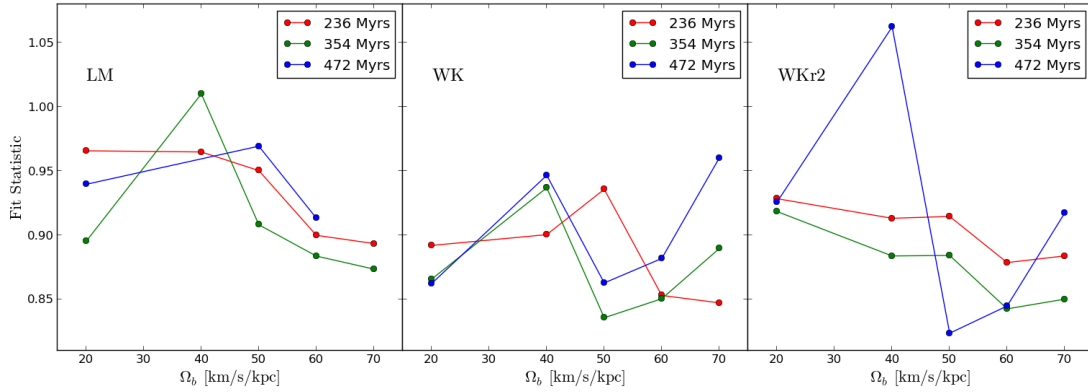


Figure 3.19: The fit to pattern speed across all bar models. There is a slight preference towards $50\text{-}60 \text{km s}^{-1} \text{kpc}^{-1}$. Note that the LM bar has a poorer fit statistic overall, and that the simulations of this bar were halted before it reached the final timestamp for $\Omega_b = 40$ and $70 \text{km s}^{-1} \text{kpc}^{-1}$.

A comparison of the fit statistic as a function of Ω_b for all our bar models at the three different time-stamps is shown in Fig. 3.19, and the best-fitting values are explicitly shown in Table 3.3. At first glance there seems to be no strong relation between the goodness of fit and Ω_b . There are however some common features between the different models. The $40\text{km s}^{-1} \text{kpc}^{-1}$ models tend to have some of the worse fits, for reasons discussed above relating to the position of arms in the outer Galaxy. The best fitting speeds tend to be in the $\Omega_b > 40\text{km s}^{-1} \text{kpc}^{-1}$ range. The best fitting pattern speed for the WK and WKr2 bars is $50\text{km s}^{-1} \text{kpc}^{-1}$, though the $60\text{km s}^{-1} \text{kpc}^{-1}$ is better fit for 2 of the 3 timestamps for the WKr2 bar, hence its inclusion as the best fitting value in

Table 3.3. While the $70\text{km s}^{-1} \text{kpc}^{-1}$ and $20\text{km s}^{-1} \text{kpc}^{-1}$ pattern speeds are numerically a good fit in some instances, we choose to not include these in our models with arm and bar potentials. This is because of the relatively short time-scale on which the l - ν emission structure appears a good match to the CO data compared to the 50 and $60\text{km s}^{-1} \text{kpc}^{-1}$ models. Figure 3.19 also indicates that overall the LM bar is a poorer fit than the model of Wada & Koda (2001), so we choose to not follow these up for further analysis in combination with arm potentials. Morphologically speaking this bar is somewhat thinner than the bar of Wada & Koda (2001) due to our choice of axis ratios. The quality of the fit could be a result of the chosen axis ratios but we do not consider this further.

Our best fitting bar models suggest a bar orientation of $\approx 45^\circ$, in accordance with observations of the ‘‘Long bar’’. In Fig. 3.20 we show the fit statistic as a function of Ω_b for the WK bar with θ_b fixed at 45° while keeping V_{obs} and R_{obs} free. The lowest fit statistics over all times considered are for the 50 and $60\text{km s}^{-1} \text{kpc}^{-1}$ models, which is consistent with the fits where θ_b is left free, and the general trend with Ω_b is similar to the WK and WKr2 bars in Fig. 3.19.

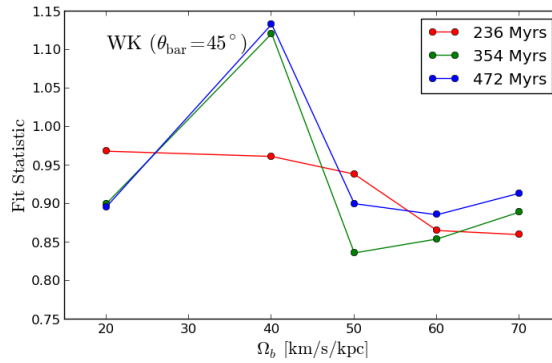


Figure 3.20: The fit statistic for the Wada & Koda (2001) bar when fixed at $\theta_b = 45^\circ$ with V_{obs} and R_{obs} left free. The simulations data is identical to that used in Fig. 3.19.

Summary of bar models

From the evidence shown above bar pattern speeds of 50 and $60\text{km s}^{-1} \text{kpc}^{-1}$ are chosen to be used further in our arm-bar mixture models. We chose to run WK bars (which appear stronger in the outer disc) at $50\text{km s}^{-1} \text{kpc}^{-1}$ and WKr2 bars at $60\text{km s}^{-1} \text{kpc}^{-1}$, the best fitting values as given in Table 3.3 for respective bars. This choice is also supported by the fit statistic shown in Fig. 3.19, which shows that 2/3 of the timestamps investigated have their minima at $50\text{km s}^{-1} \text{kpc}^{-1}$ for the WK bar and $60\text{km s}^{-1} \text{kpc}^{-1}$ for the WKr2 bar. These values are also promising as they give best-fitting values of V_{obs} and R_{obs} close to accepted literature values (Table 3.3). We do not follow up the $70\text{km s}^{-1} \text{kpc}^{-1}$ models because they lose their arm structure relatively fast compared to other models, resulting in ellipses in l - ν space. Their speed is also fast enough to sweep up a large quantity of gas inside of 4kpc . This would make it impossible for arm structures to exist in the inner Galaxy, making it difficult to see emission not associated with the elliptical bar orbits within $|l| < 45^\circ$. We exclude $20\text{km s}^{-1} \text{kpc}^{-1}$ due to their lack of any arm feature and strong inner resonance features that fail to match the morphology of the inner l - ν structure seen in the data.

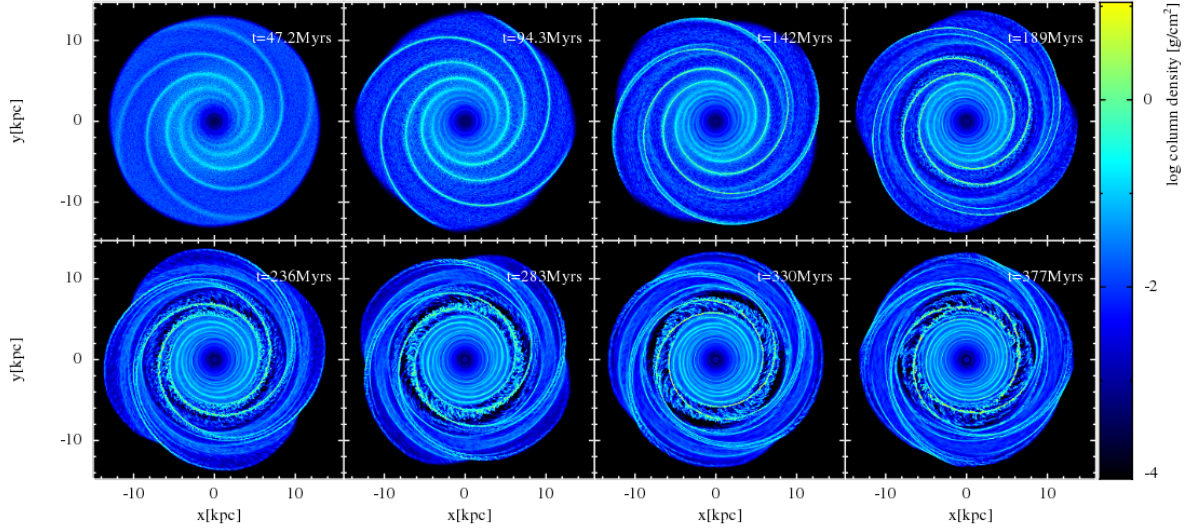


Figure 3.21: The evolution of the 4-armed model of Cox & Gómez (2002) moving at a pattern speed of $20 \text{ km s}^{-1} \text{ kpc}^{-1}$ with a pitch angle of 15° . Arm spurs are clearly seen near the ILR ($R \approx 7 \text{ kpc}$) after 200 Myrs. The outer Linblad resonance is beyond the simulation radius.

They also lack any inner features that can match the peak velocities seen in the observed CO data. The $40 \text{ km s}^{-1} \text{ kpc}^{-1}$ models are excluded due to their poorer fit statistics in the case of each model (see Fig. 3.19).

3.8 Armed simulations with cooling and chemistry

3.8.1 Simulations

An example of the evolution of an isolated CG-type arm model is shown in Figure 3.21, with the parameters; $N = 4$, $\alpha = 15^\circ$, $\Omega_{sp} = 20 \text{ km s}^{-1} \text{ kpc}^{-1}$. The spiral structure in the gas tends to survive only between the ILR and OLR region, even though the potential is present throughout the disc. For the $20 \text{ km s}^{-1} \text{ kpc}^{-1}$ case shown in Fig. 3.21 the OLR is beyond our simulation radius, but the ILR is clearly seen at later times at $R \approx 7 \text{ kpc}$. Around this radius there exists strong spur features as seen in Dobbs & Bonnell (2006). After approximately a Gyr of evolution the gas becomes aligned on 4:1 orbits at the OLR and ILR with spiral arms persisting in between. This is similar to the ring-like structures seen in the fastest bars in the previous section.

A comparison of the ISM gas response to different arm pattern speeds is shown in Figure 3.22 for our CG 2 and 4-armed models after 354 Myrs of evolution with a pitch angle of $\alpha = 12.5^\circ$. The variation with Ω_{sp} behaves in a similar fashion for different values of α . Each model has a region where spurs exist, the radial position of this decreases with increasing pattern speed and roughly corresponds with the location of the ILR. Even by-eye it is clear that some of the models in Fig. 3.22 do not display the desired morphological features. The $10 \text{ km s}^{-1} \text{ kpc}^{-1}$ $N = 4$ models all lacked spiral features that represented the underlying potential, regardless of pitch angle. While these models do show spiral structure, the gas is rotating too fast with respect

to the potential inside the ILR, resulting in a winding up of spiral features. Structure in the inner galaxy would need to be produced by the inclusion of a bar potential in this case. The fastest $N = 4$ model has the opposite problem, with a pattern speed high enough that the ILR and OLR are well inside the simulation radius (similar to bar simulations in the previous section) and there are no spiral arms in the outer disc. The slowest $N = 2$ models display very strong spur features inside of $R = 7$ kpc, with some pockets of gas maintaining a high density as it exits the arm potential. Over long time-scales this turbulent structure will form elliptical 2:1 orbital structures, similar to those seen in bar potentials.

The $N = 2$ spirals with moderate pattern speeds ($15\text{-}20\text{ km s}^{-1} \text{ kpc}^{-1}$) show evidence of supplementary spiral structure branching off the main arms. The $15\text{ km s}^{-1} \text{ kpc}^{-1}$ model in particular has a pair of branches of comparable density to those driven by the spiral potential, but of a much shallower pitch angle (second panel, top, in Fig. 3.22). These additional arm features are seen in other numerical studies of logarithmic spirals such as Patsis et al. (1994), where the bifurcation of 2 to 4 armed spirals occurs at the inner 4:1 (ultraharmonic) resonance (Patsis et al. 1997; Chakrabarti et al. 2003). The additional branching arm features seem to peak in strength around 200 Myrs, and become less defined as evolution passes 500 Myrs though are still present at much later times.

3.8.2 Simple kinematic maps

Results for a selection of arm models

A selection of l - v maps made using the method described in section 3.6 are shown in Figure 3.23. We show maps for $\alpha = 5^\circ, 12.5^\circ$ and 20° and omit those for 10° and 15° due their similarity to the 12.5° models. The upper rows show $N = 2$ models and the lower $N = 4$ models. The maps are the results of the fit to $R_{\text{obs}}, V_{\text{obs}}$ and l_{obs} similar to the previous section for the isolated bar models. Best fit parameters for the observer position and velocity are over-plotted on each map. We include no bias towards certain values of l_{obs} as we did for fitting to the bar to constrain θ_b .

l - v features are allowed to be fit by any part of the gas disc, rather than make assumptions about which l - v features should be fit by certain structures in x - y space. For instance, the local arm material was allowed to be fit to small arm branches or large primary arm structures. If the latter were the case the fit statistic should penalise the additional emission that would be present in the third quadrant but not seen in observations. As some features of the l - v maps are believed to be due to local structures, rather than a global spiral arm, it is unlikely that any single model would perfectly fit the local emission and outer arm features exactly. To investigate this, tests were made where pockets of local emission were masked out when fitting the arm models. This includes the Local arm emission ($104^\circ < l < 150^\circ, -25 < v_{los} < 15 \text{ km s}^{-1}$), the Cyg X complex ($68^\circ < l < 105^\circ, -16 < v_{los} < 30 \text{ km s}^{-1}$) and Vela region ($-106^\circ < l < -81^\circ, -14 < v_{los} < 23 \text{ km s}^{-1}$). The results of this test were somewhat inconclusive. While some models favoured a different parameter minima, the results for most were unchanged, indicating the emission for the inner quadrants was driving the fit statistic. Masking out material is not a very prudent approach, as the ability of some models to produce off-arm local material would be muted by this, which could penalise a model

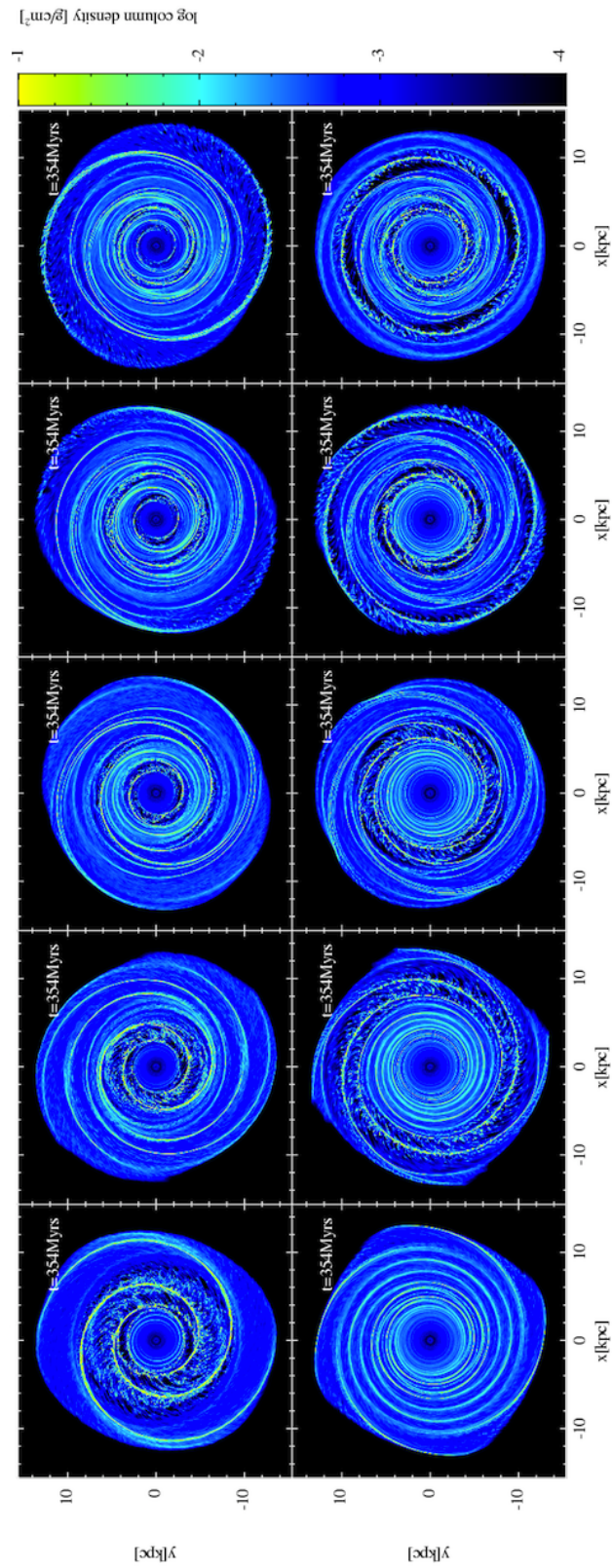


Figure 3.22: Response of the gaseous disc to arm potentials of different pattern speeds. 2-armed and 4-armed models are on the top and bottom rows respectively with increasing pattern speed along the x-axis (10, 15, 20, 25, 30 km s⁻¹ kpc⁻¹). All models are of that of Cox & Gómez (2002) after 354 Myrs of evolution with a pitch angle of 12.5°.

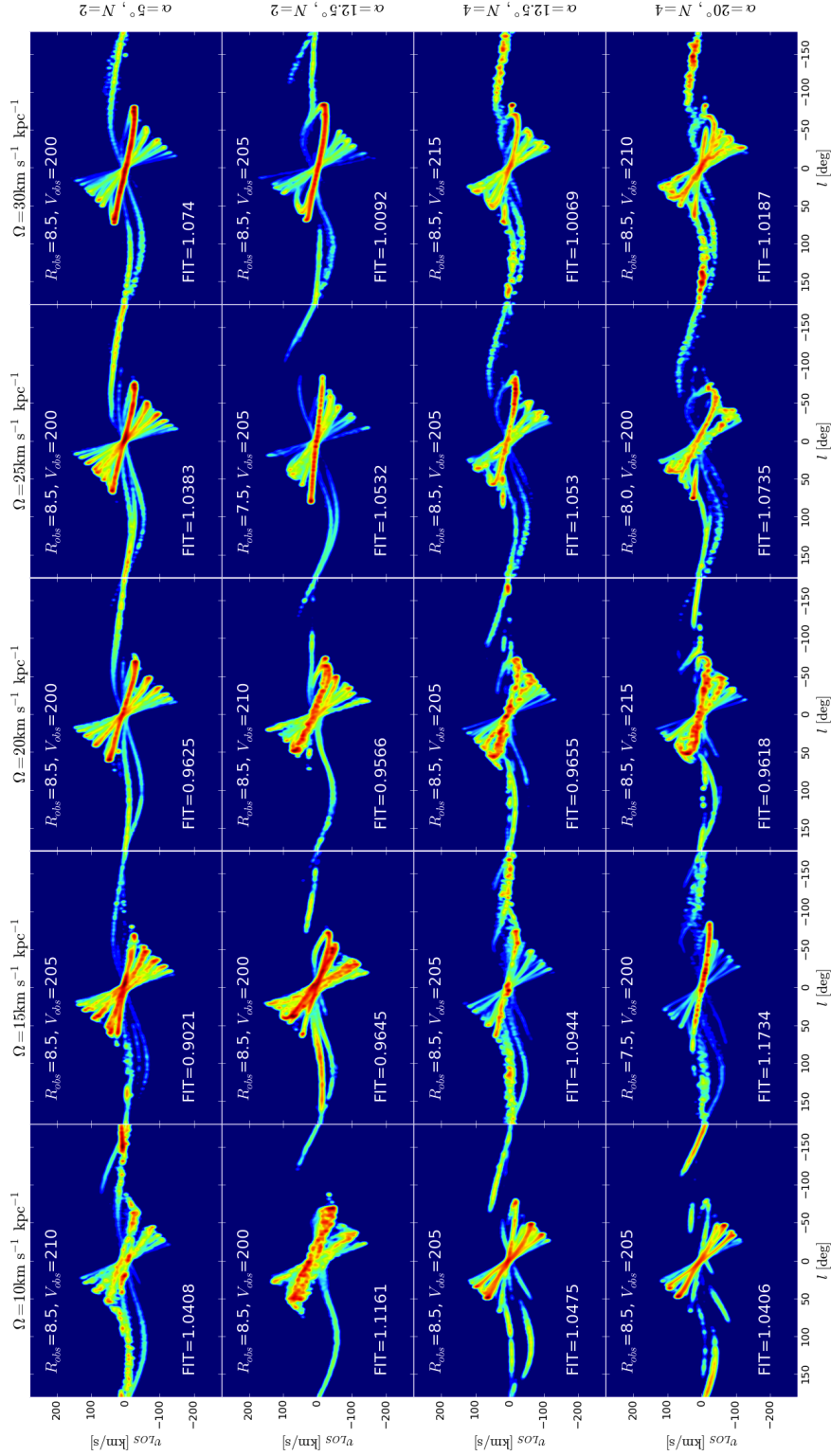


Figure 3.23: The best fit l - v maps for the arm model of Cox & Gómez (2002) rotating at pattern speeds of 10, 15, 20, 25 and 30 $\text{km s}^{-1} \text{kpc}^{-1}$ increasing from left to right with pitch angle increasing from top to bottom (5° , 12.5° and 20°). The values for the observer distance, circular velocity, and fit statistic are overplotted on each Ω_{sp} - α pair (in kpc and km s^{-1} respectively). The maps are created after the simulation has evolved for 354 Myrs. The $\alpha = 12.5^\circ$ models include both $N = 2$ and $N = 4$ morphologies. The 10° and 15° models are not shown but differ only marginally compared to the 12.5° maps.

Best fit parameter	Arm model	
	CG(N=2)	CG(N=4)
Ω_{sp} [$\text{km s}^{-1} \text{kpc}^{-1}$]	20	20
V_{obs} [km s^{-1}]	210	205
R_{obs} [kpc]	8.0	8.5
α [$^{\circ}$]	12.5	10.0

Table 3.4: Best fitting values for the arm only simulations.

that provided a good fit to all features of the l - v diagram. As such no features are masked out for any of the results shown.

General trends in the fitting are seen for all arm models. The strong local emission in the second quadrant is often fit by a major arm in the gas. The Local arm material appears significantly stronger than that of Perseus and Outer arms in the CO l - v data, giving the fit a preference to fitting to local material over the Outer arm, despite the physical size of the Outer arm being considerably greater. Fitting to the Local arm feature in l - v space causes the fit to miss the Outer arm in the second quadrant for $N = 2$ models as there is simply not enough arm structure to produce 3 distinct arms in the first and second quadrants.

Results across all arm models

The full results of our fitting to the observer's position using simple kinematic l - v maps are shown in Figure 3.24 as a function of arm pattern speed, with the best fitting values for individual parameters given in Table 3.4. The top panel shows the fit statistic for $N = 2$ models with $\alpha = 5^{\circ}, 10^{\circ}, 12.5^{\circ}$ and 15° and the bottom panel the fit to $N = 4$ models with $\alpha = 10^{\circ}, 12.5^{\circ}, 15^{\circ}$ and 20° . Only the results for the 236 and 354 Myr time-stamps are shown for clarity. We also looked at the 472 Myr time-stamp and the trends with the fit were similar. Our overall interpretation is that the $20 \text{ km s}^{-1} \text{ kpc}^{-1}$ models offer the best fit to the CO l - v data for both the $N = 2$ and $N = 4$ models. This is well within the observational bounds and is an often used value in other numerical investigations (Gerhard 2011). While $\Omega_b = 20 \text{ km s}^{-1} \text{ kpc}^{-1}$ produces the lowest fit statistic for the all models (Table 3.4) this is not as consistent over time in the $N = 2$ models compared to $N = 4$. While the best fitting values for R_{obs} are consistent with literature values, V_{obs} is slightly lower (205 and 210 km s^{-1}). This could be because the central bar is required in the central disc to better match peak inner velocity structures, forcing outer emission features to move to greater velocities and fitting to higher values of V_{obs} , nearer to 220 km s^{-1} .

The $N = 2$ arms favour a minimum of $15 \text{ km s}^{-1} \text{ kpc}^{-1}$ for the later time-stamp. Upon inspection of the individual l - v and x - y maps for this model (Fig. 3.22 and 3.23), it is apparent that the supplementary arm branches mentioned previously are the cause of this minimum. The branches are approximately 90° out-of-phase with the spiral potential and are much more apparent at 354 Myrs than 236 Myrs. These branches have a much shallower pitch angle than those being directly driven by the potential and decay before reaching the outer disc. This increase in arm features in the $N = 2$, $\Omega = 15 \text{ km s}^{-1} \text{ kpc}^{-1}$ models at later times allows for the reproduction of Perseus, Outer and Local arm features, but does not produce as strong emission in the third

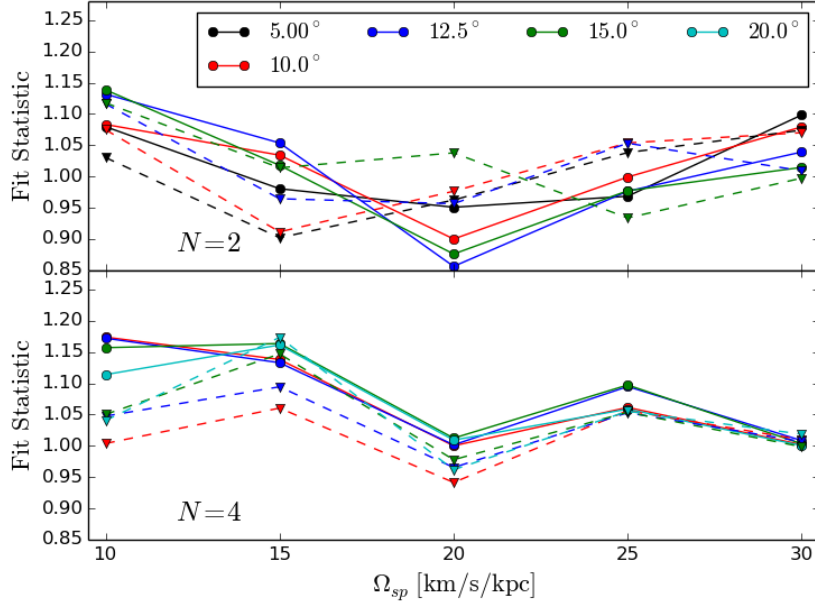


Figure 3.24: Fit statistic found by varying observer co-ordinates as a function of pattern speed of all Cox & Gómez (2002) type arm models, with various values for the pitch angle. Two different time-stamps are shown as solid (236 Myrs) and dashed (354 Myrs) lines. $N = 2$ and $N = 4$ models are shown in the upper and lower panels respectively.

quadrant as that of the $N = 4$ models (seen by comparing the $N = 2$ and $N = 4$, $\alpha = 12.5$ models). This lowers the fit statistic compared to the $N = 2$, $\Omega \neq 15 \text{ km s}^{-1} \text{ kpc}^{-1}$ models in the top panel of Fig. 3.24 at the later time stamp.

The additional arm features in the $N = 4$ models allow the reproduction of the 3 arm features seen in the observed CO data in the 1st and 2nd quadrants (Local, Perseus and Outer arms). They are also able to reproduce the characteristic “hook” in l - v space from the Carina arm in the 4th quadrant while also placing material along the Perseus and Local arms. This is seen in the $N = 4$, $\alpha = 12.5$, $\Omega_{sp} = 20 \text{ km s}^{-1} \text{ kpc}^{-1}$ model in Fig. 3.23. In order to fit to the Carina arm, there must be an arm structure placed very close to the observer’s position. For pure logarithmic spirals with constant pitch angles this will result in very bright horizontal structures in l - v space, as seen in Fig. 3.23. This is clearly at odds with the observed emission in CO (and HI), which contains no strong emission at local velocities in the inner Galaxy. There was no single arm model that could place local emission, the Carina arm and the Perseus arm in their correct places, as well as producing a strong ridge of emission angled correctly in the inner Galaxy. From Fig. 3.23 it can be seen that for any model that has a central ridge that is similar to that seen in CO observations, the Carina arm-like structure is pulled into the $|v_{los}| < 20 \text{ km s}^{-1}$ range. The resulting arm emission from the $N = 4$ models in the 3rd quadrant is detrimental to the goodness of fit, due to the lack of molecular emission in the observations. This excess emission makes the $N = 4$ models systematically worse compared to those with $N = 2$ in Figure 3.24.

Out of all parameters the pitch angle of the arms is the poorest constrained in our arm-only

models. Figure 3.24 shows no strong preference towards any given pitch angle, in the 2-armed case especially. The minima of all arm models are at 12.5° and 10° , both of which have pattern speeds of $20\text{km s}^{-1}\text{kpc}^{-1}$. At this stage there may simply be too many variables to establish a best fitting pitch angle, especially when the orientation of the arms is still a completely free parameter (determined by the best-fitting l_{obs}). The pitch angle produces fairly subtle differences in morphology compared to the arm number and pattern speed, which could explain the relatively loose correlations seen in Fig. 3.24. To try to find a stronger fit to α we attempted to fit to only the outer quadrants, where the arms should dominate the l - v structure, and negate the dominance of the central ridge in the fit statistic. The results were still inconclusive, and the fit behaved similarly as it did to the entire Galactic plane.

Summary of arm models

To further narrow down our parameter space for simulations with both arm and bar potentials we reject our $\alpha = 5^\circ$ and 20° models. By-eye inspection shows that while these models do cover a similar area of l - v space as observations, they do not trace the features correctly. The 5° models appear similar to concentric rings in l - v space, with many bright tangencies along the terminal velocity curve. The 20° models appear too wide to match features in l - v space, and stray from the potential structure at $R > 9\text{kpc}$. As there is no clear preference towards a 2 or 4 armed model seen for isolated arm simulations, we continue to use both 2 and 4-armed models in conjunction with the best bar models from the previous section. We choose to primarily use the minimum from Fig. 3.24 of $\Omega_{sp} = 20\text{km s}^{-1}\text{kpc}^{-1}$ for further arm simulations. We also include 2-armed, $\Omega_{sp} = 15\text{km s}^{-1}\text{kpc}^{-1}$ potentials due to the secondary minimum in Fig. 3.24.

It is clear from the results shown here that the pattern speed is an extremely important parameter for any arm/bar model of the Milky Way, perhaps as important as arm number or bar orientation. Especially in the case of the bar, where it dictates the radial extent of the bar, more so that the actual bar length incorporated into the potential. Regardless of the presence of a stellar potential, the pattern speed dictates whether the gas will trace the potential, due to the radial placement of resonance features. Figure 3.25 shows the position of a stellar potential and the gaseous response (top), along with the potential's projection in l - v space and the synthetic l - v map of the gas. While the outer arms trace the potential well (both in x - y and l - v space) the inner disc is devoid of structure, and the pitch angle is increasingly wound up as you approach the galactic centre. The arms have been orientated to reproduce the Carina tangency in the 4th quadrant. For cases such as these where the arms seem well represented in the outer disc there is little structure in the inner Galaxy. This means that in these cases emission in the inner Galaxy needs to be driven by the inclusion of a bar potential, leading to the conclusion that both arm and bar features are needed to fully represent Galactic emission. Having differing pattern speeds for each would especially help the $N = 2$ case, as it would allow molecular structures to exist throughout the disc (as two $m = 2$ potentials moving at the same pattern speed would span the same radial domain).

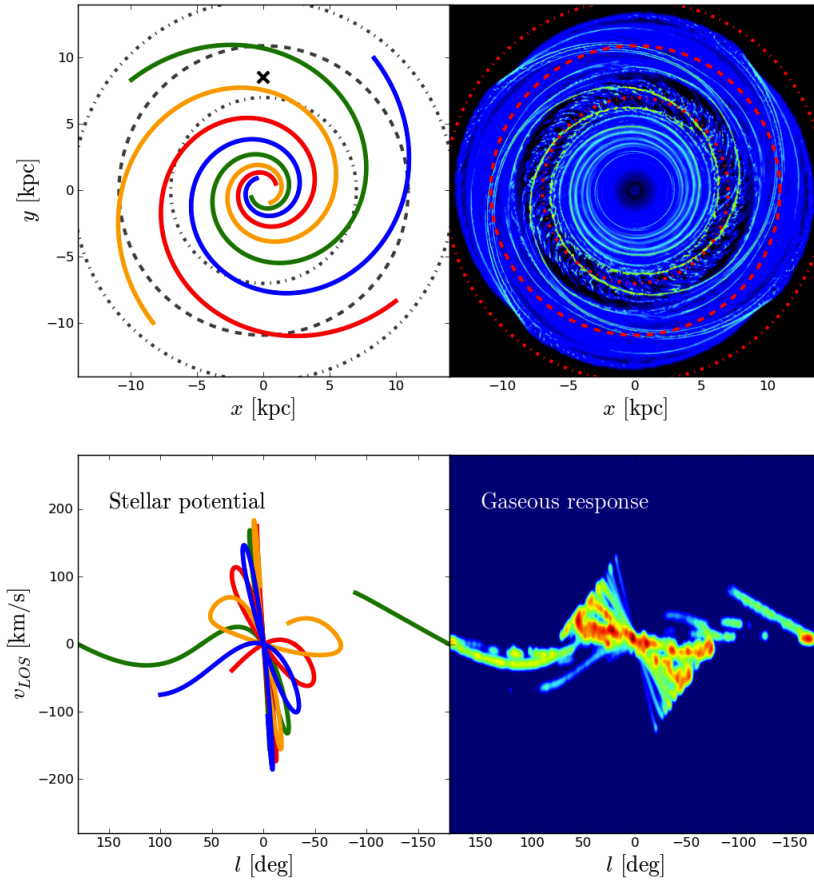


Figure 3.25: Illustration of the arm locations in simulations resulting from positions of resonances. Top: 4-armed spiral model moving at $20\text{km s}^{-1} \text{kpc}^{-1}$ with $\alpha = 12.5^\circ$ after 354Myrs of evolution (left) and the position of the spiral stellar potential (left). Dashed circles show the locations of the ILR, CR and OLR in order from centre. Bottom: the location of the spiral potential in l - v space (right) and the gaseous response in the simulation (right). Note the lack of spiral structure inside the ILR and subsequent absence in l - v space.

3.8.3 Arm strength

In addition to the standard CG spiral arms we performed calculations with arm potentials with double the strength of our fiducial value. The purpose of which was to improve the gas tracing of the potential, as in some instances in the models shown in Figure 3.22 the gas only weakly traces the imposed arm structure. For example, the $N = 2$ models have significant branches at moderate pattern speeds, and the highest density gas is not exclusively associated with the bottom of the spiral potential, even within the ILR and OLR. Figure 3.26 shows stronger arm models with double the fiducial arm strength, with 2 or 4 arms (top and bottom rows) and pattern speeds of 15 , 20 and $25\text{km s}^{-1} \text{kpc}^{-1}$. The best fitting l - v maps are shown in Figure 3.27. These can be directly compared with the central six panels in Figure 3.23, which have the same pitch angle, pattern speed and arm number (though have evolved for slightly longer). Characteristic 4:1 and 2:1 resonant orbits become clear much earlier in this simulations with increased potential

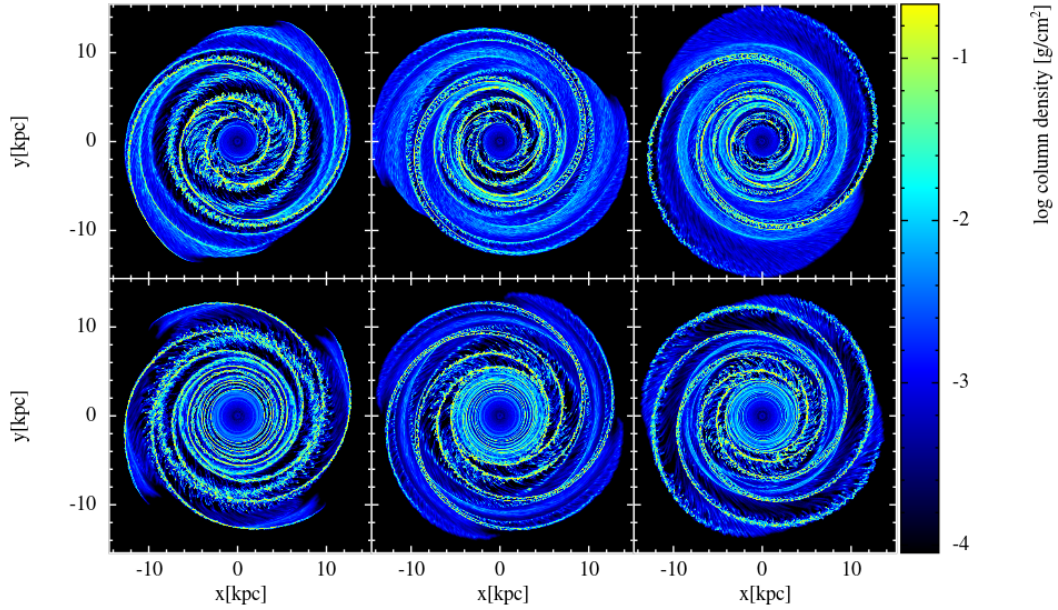


Figure 3.26: Calculations with double the normal arm potential strength with $N = 2$ (top) and $N = 4$ (bottom). The pattern speed varies from $15\text{-}25\text{ km s}^{-1} \text{ kpc}^{-1}$ from left to right. The calculations were performed up to 236 Myrs . These can be compared to calculations with the standard potential strength shown in the central panels of Figure 3.22.

strength (even more so considering these have had less time to evolve). The 2:1 and 4:1 orbits can clearly be seen in the $15\text{ km s}^{-1} \text{ kpc}^{-1}$ calculations. Other than this difference the over-all morphology is the same. This can be seen by comparing between $l\text{-}v$ plots. The $20\text{ km s}^{-1} \text{ kpc}^{-1}$ maps are extremely similar for both arm strengths, and still provide the best fit out of these models compared to the 15 and $25\text{ km s}^{-1} \text{ kpc}^{-1}$ models. These other speeds show slight differences. The $N = 2$, $\Omega_{sp} = 15\text{ km s}^{-1} \text{ kpc}^{-1}$ model has lost some arm structure in $l\text{-}v$ space, a result of the arm branches being wrapped up into 2:1 orbits much faster than the standard strength models. The $N = 2$, $25\text{ km s}^{-1} \text{ kpc}^{-1}$ model provides a better $l\text{-}v$ map in the stronger case, due the additional potential strength sweeping up gas much more effectively in the outer disc.

These models with stronger arms do not show dramatic differences to our standard strength models, and provide the same best fitting pattern speed (though only the central 3 values were checked). A single arm strength was adopted for use for arm-bar mixed calculations, with some confidence that $l\text{-}v$ features will not change greatly if a stronger potential were used.

3.8.4 Complex spiral arm model

Calculations using the PM arm model were made using a single pattern speed of $20\text{ km s}^{-1} \text{ kpc}^{-1}$ and pitch angle of 12° to investigate the plausibility of a four armed gas response to a two armed potential. This potential also decays away much faster with radius than the CG model. Figure 3.28 shows calculations with a spiral masses of $1.5 \times 10^9 M_\odot$ at 236 (top left), 354 (bottom left) and 472 (bottom right) Myrs. Also shown is a calculation with a larger spiral mass of $2.6 \times 10^9 M_\odot$

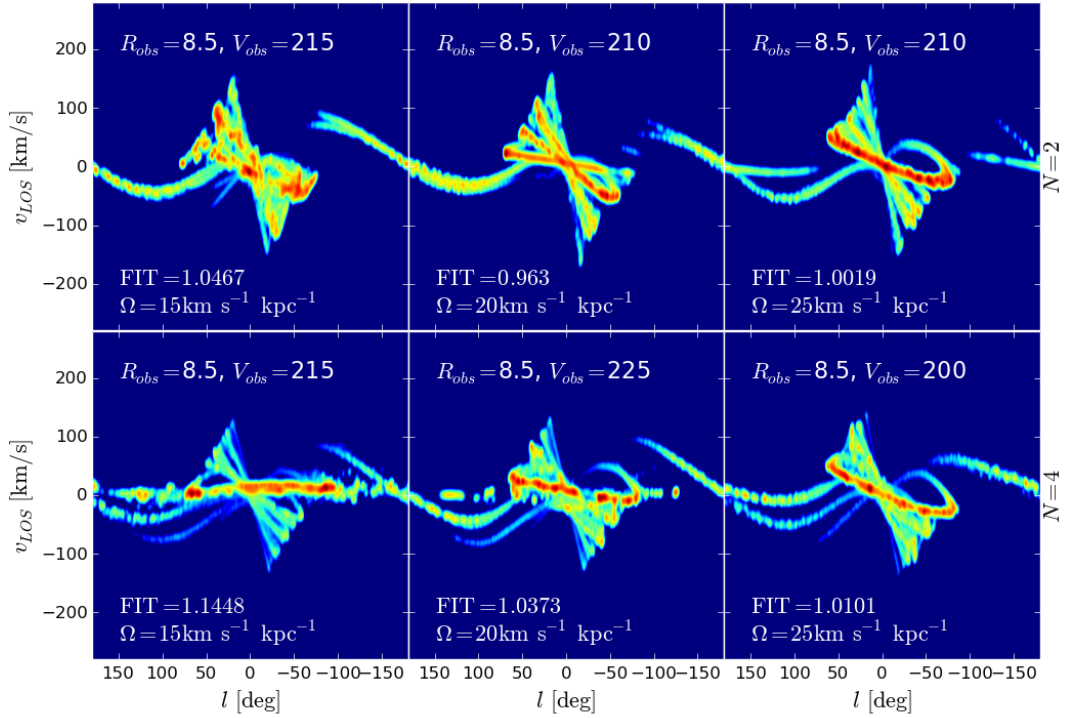


Figure 3.27: Best-fitting l - v maps of the calculations shown in Figure 3.26. These can be compared to calculations with the standard potential strength shown in the central panels of Figure 3.23.

(top right panel). In Pichardo et al. (2003) the authors state the supplementary arm features are stronger in the lower mass case. The figure shows that the PM arms do indeed drive additional arm structures, appearing strongest in the mid-Galactic disc in the top left panel. These supplementary arms seem to exist between the ILR and 4:1 resonance, located at approximately 8kpc. These additional spiral branches have shallower pitch angles than the arms driving their formation, and are nearly circular approaching the Solar radius. At later times the PM resonant arms become less pronounced, and the 4:1 resonance begins to dominate the flow of gas around $R = 6$ kpc (the same position as the ILR of 4-armed models). Increasing the strength of the spiral potential makes little difference to the gas response, with the main effect being the additional spurring near the ILR ($R < 2$ kpc).

Arm branches are also present in the $N = 2$, CG models (upper panels in Fig. 3.22). The branches in the PM arms are slightly stronger than those seen in the CG potential, but the primary arms in the PM model are relatively weaker than those of the CG potential. In the CG arms these are more pronounced in the $15\text{km s}^{-1}\text{kpc}^{-1}$ calculations, though can still be faintly seen when $\Omega_{sp} = 20\text{km s}^{-1}\text{kpc}^{-1}$. Calculations with this lower pattern speed were also performed for the PM model, and supplementary arm features are even stronger in the outer disc, but all arm structure is weaker at intermediate disc radii $R \approx 8$ kpc.

The main features of this model were also studied in Gómez et al. (2013), where the authors also found supplementary arm features with shallow pitch angles. However, in their study the supplementary arms maintain a form similar to that to the top left panel in Figure 3.28 for up to

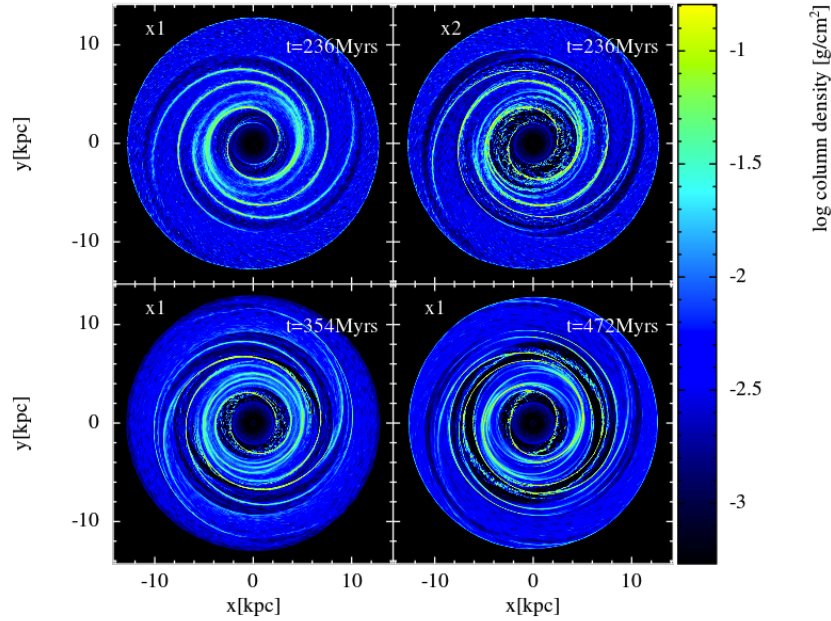


Figure 3.28: Two calculations with the PM spiral arm potential. A calculation with the fiducial arm strength is shown at three separate times in the top left, bottom right and bottom left panels. The top right shows a calculation with twice the fiducial arm strength at a time of 236 Myrs.

4 Gyrs, whereas we find these structures short lived. A possible explanation for this is that the calculations of Gómez et al. (2013) are isothermal at $T = 8000\text{K}$, which is considerably hotter than the gas in our calculations with active cooling. Figure 3.5 shows that isothermal calculations of the order $T = 10000\text{K}$ produce a much smoother gaseous response, and trace the underlying potential much clearer than their 200K counterpart.

Figure 3.29 shows the best-fitting l - v maps of the models shown in Figure 3.28, where the disc is angled so that the observer is placed at $(0, R_{\text{obs}})$. It is clear that although the arms display a 4 armed pattern in some cases, there is little arm structure in most of these maps, with the slight exception of the stronger arm case. The arms replicate the inner ridge of emission from the arm closest to the observer, but fail at reproducing the outer arm structures. This is due to the arm structures being confined to relatively small radii, while the Outer and Perseus emission comes from radii larger than the extent of the spiral structures shown in Figure 3.28. Using this potential with a pattern speed of $15\text{km s}^{-1} \text{kpc}^{-1}$ it is possible to create arm features in the outer disc. However, at this speed the CG arms also provide strong secondary arm features, negating the benefit of using this complex potential. As this arm model provides no significant benefit to the CG arm model it is removed from our refined parameter space for use with bar potentials. Some preliminary calculations were made with this potential in combination with the WK bar model. Due to radially constrained nature of the PM arms they were heavily disrupted by the inclusion of a bar, making them even less suitable as a representation of the Milky Way’s spiral structure.

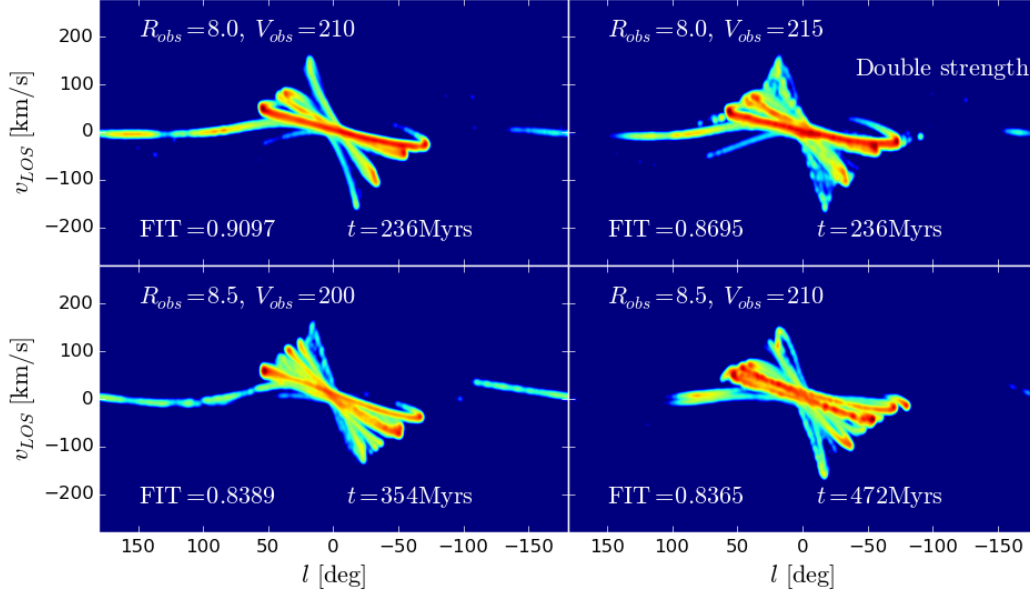


Figure 3.29: The best-fit l - v maps for the calculations shown in Figure 3.28, with best-fit parameters indicated in each corresponding panel. The discs in Figure 3.28 have been orientated such that the observer is located at $(0, R_{\text{obs}})$ in the construction of these maps.

3.9 Chapter summary

In this chapter we have presented calculations of the evolution of ISM gas embedded in various stellar potentials representing the Galactic arms and bar. These include simple sinusoidal perturbations of the Galactic disc, and more complex models formulated from a density profile tailored to specific Milky Way mass components. The ISM embedded within these potentials has very diverse responses depending on pattern speed, which appears to be a key factor in determining the radial extent of the gaseous response.

In order to narrow down the hefty parameter space defining the exact morphology of these potentials we formulated a method of creating l - v maps that, while simplistic in nature, allowed for a very fast sweep through parameter defining the observers position and velocity. Using this technique allowed for the creation of a much narrower parameter space for use in calculations with active bar *and* spiral potentials. Best-fitting bar models favoured fast rotations, and orientation angles of approximately 45° , within agreement with values found for the “Long Bar”. The best-fitting arm models seem only weakly dependent on pitch angle, but showed a clear minima for pattern speeds of $20\text{km s}^{-1} \text{kpc}^{-1}$, also in agreement with values suggested in the literature. There is only a weak preference to a 2 over a 4 armed model regarding the values of the fit statistic, with each showing clear differences in l - v structures. The 4-armed models were however the only ones capable of reproducing all l - v features, the 2-armed models simply could not seem to produce enough emission structures in l - v space. The downside being that they produce too much emission where it is not needed.

The possibility of a 2 armed stellar spiral driving a 4 armed gas structure was also investigated. A slightly slower pattern speed of $15\text{km s}^{-1} \text{kpc}^{-1}$ showed strong and long-lasting supplementary arm features. A complex arm model that is very efficient at creating supplementary arm features was investigated, but did not show a clear benefit to simpler arm models we have been using.

In the next chapter the refined arm/bar parameter space will be used in calculations with barred-spiral simulations, with the aim of producing an $l-v$ map that produces all features observed in observations. As our parameter space is now much smaller, and we are approaching a global best-fit model, we will be employing a radiative transfer code to fully model the molecular emission of the ISM, as opposed to the simple maps used in this chapter.